

This is the preprint of the contribution published as:

Bloise, Andrea, Manuela Catalano, Eugenio Barrese, Alessandro Francesco Gualtieri, Nicola Bursi Gandolfi, Silvana Capella, and Elena Belluso. 2015. 'TG/DSC Study of the Thermal Behaviour of Hazardous Mineral Fibres'. *Journal of Thermal Analysis and Calorimetry* 123 (3): 2225–39. doi:10.1007/s10973-015-4939-8.

The publisher's version is available at:

<http://link.springer.com/article/10.1007/s10973-015-4939-8>

When citing, please refer to the published version.**Link to this full text:**

<http://hdl.handle.net/2318/1567980>

This full text was downloaded from iris-AperTO: <https://iris.unito.it/>

1
2 **TG/DSC study of the thermal behaviour of hazardous mineral fibres**
3
4
5
6

7 A. Bloise^a, M.Catalano^a, E. Barrese^a, A. F. Gualtieri^b, N. Bursi^b, S. Capella^c, E. Belluso^{c,d,e}
8
9

10
11
12
13
14 a) Dipartimento di Biologia, Ecologia e Scienze della Terra, Università della Calabria, Via Pietro Bucci, Cubo 15b,
15 87036 Rende, Italy
16

17
18
19 b) Dipartimento di Scienze Chimiche e Geologiche, Università di Modena e Reggio Emilia, Via S. Eufemia 19, I-41121
20 Modena, Italy
21

22
23 c) Dipartimento di Scienze della Terra, Università di Torino, Via Valperga Caluso 35, 10125 Torino, Italy
24

25
26 d) CNR, Istituto di Geoscienze e Georisorse, Unità di Torino, Via Valperga Caluso 35, 10125 Torino, Italy
27

28
29 e) Nanostructured Interfaces and Surfaces, Centro Interdipartimentale di Eccellenza, Università di Torino, Italy
30
31

32
33
34
35
36 Corresponding author

37 Andrea Bloise,

38 Dipartimento di Biologia, Ecologia e Scienze della Terra - Università della Calabria, Via Pietro Bucci, Cubo 15b,
39 Rende, 87036, tel./fax. +390984 493588,
40

41 e-mail: andrea.bloise@unical.it
42
43
44
45
46
47
48
49
50
51
52
53
54
55
56
57
58
59
60
61
62
63
64
65

ABSTRACT

1
2 For the first time, this paper reports a systematic and comparative study of the thermal behaviour of
3
4 fibres of social, health, economic and industrial relevance using thermogravimetric and differential
5
6 scanning calorimetry (TG/DSC). The mineral fibres selected for the study are: three chrysotiles
7
8 samples, crocidolite, tremolite asbestos, amosite, anthophyllite asbestos and fibrous erionite.
9
10 Powder X-ray diffraction (PXRD) and scanning electron microscopy combined with energy
11
12 dispersive spectrometry (SEM/EDS) were used for the characterization of the mineral fibres before
13
14 and after heating at 1000 or 1100 °C to identify the products of the thermal decomposition at a
15
16 microscopic and structural scale and characterize their thermal behaviour.
17
18
19
20

21 TG/DSC data allowed the determination of the structural water content and temperature stability.
22

23
24 Furthermore thermal analysis provided a sensitive and reliable technique for the detection of small
25
26 quantities of different mineral phases occurring as impurities. After thermal treatment, fibrous
27
28 samples were completely transformed into various iron oxide, cristobalite and other silicate phases
29
30 which preserved the original overall fibrous morphology (as pseudomorphosis). Only crocidolite at
31
32 1100 °C was partially melted and an amorphous surface was observed.
33
34
35
36
37
38

39 *Keywords:* Mineral fibres, Asbestos, Thermal behaviour, Dehydroxylation, Pseudomorphosis.
40
41
42

Introduction

43
44 Among the minerals which are considered particularly hazardous for human health, the most
45
46 notorious display a fibrous-asbestiform crystal habit [1]. It is now widely accepted to include in the
47
48 family of the so-called asbestos mineral the following species: serpentine chrysotile, five amphibole
49
50 species named tremolite and actinolite asbestos, crocidolite, amosite, anthophyllite asbestos and the
51
52 fibrous zeolite erionite [2].
53
54
55
56
57
58
59
60
61
62
63
64
65

1 Chrysotile is a member of the serpentine group, a 1:1 layer silicate (constituted by a tetrahedral and
2 a trioctahedral sheet) whose layers are rolled so to assume a characteristic fibrous habit [3, 4].
3

4 Amphiboles are double-chain silicates which may display a fibrous habit being structurally
5 elongated in one preferred crystal direction. Finally, erionite is a common fibrous/acicular zeolite
6 with an hexagonal, cage-like structure composed of a framework of linked tetrahedral [5, 6].
7

8 Despite their outstanding technological properties (e. g. low thermal conductivity, high mechanical
9 strength, workability, among the others) which prompt their widespread industrial applications,
10 asbestos minerals are considered hazardous. In general, all asbestos fibres if inhaled are thought to
11 induce malignant mesothelioma, lung cancer (in combination with other factors), and other lung
12 diseases [7, 8]. According to the existing regulations, amphibole asbestos fibres are banned
13 worldwide whereas chrysotile is banned in only 28% of the countries worldwide. In the other
14 countries, safe use of chrysotile is admitted. Asbestos erionite unfortunately is not regulated but
15 listed by International Agency for Research of Cancer (IARC) as substance carcinogenic to humans.
16

17 As a matter of fact, *in vivo* studies unequivocally proved that asbestiform erionite is more
18 tumorigenic than chrysotile and crocidolite asbestos [9].
19

20 Since the advent of industrial age, asbestos fibres have been extensively used in an endless number
21 of industrial applications and especially to manufacture various types of artefacts (asbestos cement,
22 disc brake pads, pipes, reinforcing agents, fire retardants etc). In those countries where all asbestos
23 minerals are banned, and remediation policies are fostered, many attempts were made to detoxify
24 asbestos minerals by using different techniques [10-12]. In this regard, many projects and patents
25 have dealt with the possible disposal and re-use of asbestos-containing materials (ACM) via the
26 crystal-chemical transformation induced by thermal treatment [13-18]. However, it must be
27 considered that the thermal transformations sequence of asbestos-containing materials (ACM),
28 composed of a variety of different crystalline and amorphous phases, is totally different with respect
29 to the transformations sequence of pure asbestos minerals.
30

1 Concerning pure chrysotile, it has been demonstrated that its structure collapse at around 650 °C
2 with early recrystallization at about 800 °C into anhydrous silicates such as forsterite and
3
4 amorphous silica [19]. With respect to chrysotile, papers dealing with the thermal decomposition of
5
6 pure amphibole asbestos and erionite are rare. As a matter of fact, only few studies were devoted to
7
8 the thermal decomposition of pure amphibole asbestos up to 1100 °C and rare data report on the
9
10 new phases appeared after thermal treatment. Thermal decomposition of fibrous amphibole
11
12 minerals have been generally limited to asbestos minerals of commercial value or health concern
13
14 such as crocidolite [20-25] and amosite [23, 26, 27]. Moreover, in some papers regarding the
15
16 thermal analysis of amphiboles asbestos, a full picture of their thermal behaviour is not given [28].
17
18 Regarding erionite, the thermal behaviour of a sample from Jersey Nevada (USA) is described in
19
20 only one paper [29] which showed that the main endothermic event has occurred at about 140 °C
21
22 but did not report the TG curve neither the temperature of the structural collapse.
23
24
25 In this scenario, the aim of this study was to systematically investigate and compare the thermal
26
27 behaviour (TG/DSC) as well as the phase transformations of the most relevant mineral fibres during
28
29 heating up to 1000 or 1100 °C. The study was performed on eight selected fibrous minerals
30
31 including chrysotile, crocidolite (asbestiform riebeckite), tremolite asbestos, anthophyllite asbestos,
32
33 amosite (grunerite asbestos) and fibrous erionite object of many important biomedical studies [30,
34
35 31]. Four fibrous species (chrysotile, crocidolite, amosite, and anthophyllite asbestos) were
36
37 distributed by the International Union Against Cancer (UICC).
38
39
40 The deep knowledge of thermal behaviour of these asbestos minerals may deliver data relevant for
41
42 the understanding of the crystal-chemical transformations of asbestos through thermal treatment and
43
44 for the identification of asbestos mineral fibres in bulk natural samples using TG/DSC.
45
46
47 Furthermore, since both asbestos samples and asbestiform erionite are used for *in vitro* studies to
48
49 test their cyto-toxicity [30, 31], the determination of the presence of impurities may be crucial as
50
51 such contaminants may adversely affect the experimental results.
52
53
54
55
56
57
58
59
60
61
62
63
64
65

Materials and methods

Table 1 reports the nature and chemical formula (after Pollastri et al., 2015 [32]) of the eight investigated fibres: UICC chrysotile from Canada; chrysotile from Balangero (Italy); chrysotile from Val Malenco (Italy); UICC crocidolite from Koegas Mine, Northern Cape (S. Africa); tremolite asbestos from Val d'Ala (Italy); UICC amosite from Penge mine, Northern Province (S. Africa); UICC anthophyllite asbestos from Paakkila (Finland) and asbestiform erionite from Jersey Nevada (USA). The major focus of the work was to systematically characterize the mineral fibres by thermal analysis specifically thermogravimetric (TG), derivative thermogravimetric (DTG), differential scanning calorimetry (DSC), derivative differential scanning calorimetry (DDSC). TG and DSC were performed in an alumina crucible under a constant nitrogen flow of $30 \text{ cm}^3 \text{ min}^{-1}$ with a Netzsch STA 449 C Jupiter in a 25 – 1000 and 25 -1100 °C temperature range, with a heating rate of 10 °C/min. Instrumental precision was checked by six repeated collections on a kaolinite reference sample revealing good reproducibility (instrumental theoretical T precision of $\pm 1.2 \text{ }^\circ\text{C}$) and theoretical weight sensitivity of 0.10 μg , DSC detection limit $< 1 \mu\text{W}$. Samples were powdered by dry-grinding in an agate mortar; about 40 mg of each sample were used in all collections. Owing to the remarkable length of the chrysotile fibres from Val Malenco, before grinding they were cut with scissors.

A qualitative phase analysis, both of natural and heated samples, was performed according to the powder X-ray diffraction method (PXRD) using a Bruker D8 Advance X-ray diffractometer at 40 kV and 40 mA. The instrument is equipped with a copper tube and curved graphite monochromator. Scans were recorded in the range of 3–66 $^\circ 2\theta$, with a step interval of 0.02 $^\circ 2\theta$ and a step-counting time of 3 s/step. EVA software (DIFFRACplus EVA) was used to identify the mineral phases and experimental peaks being compared with the 2005 PDF2 reference patterns. The morphology of the samples before and after thermal analysis was investigated by scanning electron microscopy (SEM)

1 using an Environmental Scanning Electron Microscope FEI QUANTA 200 equipped with an
2 EDAX Genesis 4000 energy dispersive X-ray spectrometer (EDS), and a FEI Nova NanoSEM 450
3
4 equipped with an X-EDS Bruker QUATAX-200 system for the microanalysis.
5
6
7
8

9 **Results and discussion**

10 *Chrysotile*

11
12 The thermal analysis for chrysotile UICC (Fig. 1) showed four endothermic peaks at 226, 401, 520
13
14 and 633 °C. The first peak at 226 °C may be due to the dehydroxylation of pyroaurite [33]; the peak
15
16 and 633 °C. The first peak at 226 °C may be due to the dehydroxylation of pyroaurite [33]; the peak
17
18 at 401 °C to the dehydroxylation of brucite and de-oxygenation of pyroaurite [33, 34]; the very
19
20 weak peak at 520 °C is thought to be generated by the decarbonation of siderite [35], likely present
21
22 as very minor impurity; the wide peak at 633 °C to the chrysotile dehydroxylation [22, 36]. The
23
24 weak endothermic event at 901 °C on DTG (Fig. 1) curve was ascribed to talc dehydroxylation [37,
25
26 38]. It is possible that the wide endothermic event at 633 °C hides minor endothermic events due to
27
28 the decarbonation of calcite, dolomite, and/or dehydroxylation of clinocllore [34, 36, 37].
29
30
31
32

33
34 The TG curve showed a weight loss of 0.91 % below 110 °C due to adsorbed water while the main
35
36 weight loss of 12.22 % was due to chrysotile dehydroxylation (Table 2).
37

38
39 Our findings are in line with previous literature data on chrysotile dehydration mechanisms and
40
41 high-*T* crystallization [39-42]. The product of the dehydroxylation of chrysotile recrystallized to
42
43 forsterite [19, 43, 44] caused a sharp exothermic peak at 823 °C (Fig. 1, Table 3). Indeed, the
44
45 corresponding PXRD pattern (Fig. 2) of the chrysotile UICC after thermal treatment confirmed the
46
47 presence of the forsterite.
48
49

50
51 The DSC curve of the chrysotile from Balangero exhibited one major effect (Fig. 3) at 660 °C
52
53 related to the chrysotile dehydroxylation with a weight loss of 11.80 %. As already described above,
54
55 the weak endothermic effect (Fig. 3, Table 3) at 402 °C is due to brucite [34] breakdown. In the
56
57 DTG curve the peak at 869 °C was related to the decarbonation of dolomite [45]. The DSC weak
58
59
60
61
62
63
64
65

1 shoulder effect at 938 °C which was clearly recorded on DDSC curve was related to the talc
2 dehydroxylation [38]. Again, the wide endothermic event at 660 °C may hide minor endothermic
3 events due to the I decarbonation of dolomite, calcite, and clinocllore [34, 36, 37]. The weak
4 endothermic effect at 717 °C visible on the DTG curve (Fig. 3) is due to the antigorite
5 dehydroxylation [36, 46]. The effect on TG curve (- 0.57 wt%) below 110 °C was ascribed to the
6 release of humidity adsorbed at the sample surface while the total weight loss at 1000 °C was of
7 14.9 % (Table 2). On the DSC curve the exothermic peak at 822 °C (Fig. 3) was related to the
8 crystallization of forsterite as determined by PXRD after thermal treatment at 1000 °C (Fig. 2).
9 The TG curve for the chrysotile from Val Malenco (Fig. 4) showed a continuous weight loss mainly
10 due to the decomposition of chrysotile in correspondence with the major endothermic event at 652
11 °C (see the DSC curve in Fig. 4). Dehydroxylation of chrysotile causes a weight loss of 12.01 %.
12 DTG weak effect at 760 °C (Fig. 4) is the diagnostic signal [47] of the presence of antigorite in the
13 sample which was also detected by TEM analysis on the same sample by Cattaneo et al. [48]. Broad
14 DTG and DSC signals in the 25–110 °C range were due to adsorbed water (weight loss of 0.54 %)
15 while the total weight loss at 1000 °C was 13.35 % (Table 2). A sharp exothermic peak at 820 °C
16 indicates the crystallization of forsterite [19, 43, 44] as confirmed by PXRD data (Fig. 2).
17 As showed in Fig. 5 the curves of the three chrysotile samples have similar trend; no significant
18 variation in the exothermal peaks (range 820-823 °C) was observed, while a slight difference in the
19 main endothermic effect occurred. The endothermic peak observed for the chrysotile UICC shows a
20 shift versus lower temperature (633 °C) with respect to both chrysotile from Val Malenco (652 °C)
21 and chrysotile from Balangero (660 °C). The different temperature of chrysotile decomposition
22 (range 633-660 °C) of the three chrysotile samples may be due to the different fibre size (width and
23 length) distribution and the presence of different amount of Fe [43, 49] and Ni [44] substitute for
24 Mg in octahedral sheet [32]. The relationships between distribution size, Ni, Fe content and change
25 of temperature stability of chrysotile are complex. In fact, as recently demonstrated, the thermal
26
27
28
29
30
31
32
33
34
35
36
37
38
39
40
41
42
43
44
45
46
47
48
49
50
51
52
53
54
55
56
57
58
59
60
61
62
63
64
65

1 shift in chrysotile decomposition can be also related to the presence of trace elements in its structure
2 (i.e. Li, As, Sb) [50] which may control the range of temperature over that the structure collapses.
3
4 The TG curves of the three specimens of chrysotile showed a weight loss of about 12 % (Table 2)
5
6 due to their decomposition [19, 51]. These data match the theoretical and experimental values of
7
8 mass loss observed in natural and synthetic chrysotile fibres reported in literature [19, 43, 47, 51].
9
10 A representative set of secondary electron SEM images showing the morphology of chrysotile
11
12 before and after thermal analysis at 1000 °C is reported in Fig. 6. The unheated fibres of chrysotile
13
14 samples appear arranged in bundles (Fig. 6a, 6d) and curved with their typical wavy appearance
15
16 (Fig. 6g). The splitting in fibrils starting from the fibre bundle is shown in Figures 6a and 6d . After
17
18 thermal treatment at 1000 °C, chrysotile fibres recrystallize in forsterite apparently retaining the
19
20 original fibrous crystal habit (pseudomorphosis phenomenon) [52, 53] and appearing curved and
21
22 still flexible (Fig. 6b, 6e, 6h). However, at higher magnification (HM) the apparent fibres turn out to
23
24 be a continuous sequence of sub-cylindrical particles with basis both sharp and perpendicular to the
25
26 original fibre axis [16], approximately 100 nm in length (Fig. 6c), Sometimes, the new silicate is
27
28 constituted by sub-spherical particles disposed not very tidily along the axis (Fig. 6f). The original
29
30 cleavage parallel to the fibre axis is lost (Fig. 6c). Therefore, the eventual fracture of the
31
32 transformed pseudo-morphic fibres occurs at the particle boundaries and not along the fibre axis.
33
34 Moreover, as observed in Fig 6i, the typical smooth surface of chrysotile fibres is completely lost
35
36 becoming very rough.
37
38
39
40
41
42
43
44
45
46
47

48 Amphiboles

49 *Crocidolite*

50
51 The DTG curve of crocidolite (Fig. 7) shows a major endothermic event at 648 °C related to iron
52
53 oxidation accompanied by dehydrogenation and/or dehydroxylation. The structure does not show
54
55 collapse which occurs at higher temperature [24] with a corresponding weight loss of 2.18 % in the
56
57
58
59
60
61
62
63
64
65

1 range 110-680 °C of the TG curve. No weight loss of crocidolite was observed above 700 °C in
2 agreement with Fujishige et al. [54]. As it can be observed in the DTG curve (Fig. 7), the partial
3 oxidation of ferrous iron content in the crocidolite takes place in the range 200-580 °C [55], as
4 confirmed by the three weight gain peaks at 205, 360, and 570 °C (Fig. 7). Although the detailed
5 discussion of the processes is not the object of this paper, it is necessary to point out that the
6 oxidation of crocidolite is essentially a dehydrogenation, as long as dehydroxylation occurs [21] so
7 that the mechanism of oxidation was considered to be dependent on migration of protons and
8 electrons through the crystal. Indeed, when hydrated silicates containing ferrous iron are heated the
9 constitutional hydroxyl decomposes and iron may change its valence state. Oxidation may result
10 from either the incorporation of oxygen into the material (oxygenation) or a dehydrogenation with
11 the following mechanism: $\text{Fe}^{2+} + \text{OH}^- \rightarrow \text{Fe}^{3+} + \text{O}^{2-} + \text{H}$ [56].
12
13
14
15
16
17
18
19
20
21
22
23
24
25
26

27 The DSC curve up to 700 °C showed two exothermic and two endothermic effect: 320 °C, 431 °C,
28 354 °C and 649 °C respectively (Table 3). The first exothermic effect at 320 °C was related to the
29 crocidolite dehydrogenation as confirmed by the weight gain peak at 360 °C in the DTG curve due
30 to consequent Fe^{2+} oxidation. The endothermic effect at 354 °C should be related to the
31 dehydroxylation of hydroxyl water of the crocidolite with a consequent formation of oxy-crocidolite
32 (crocidolite partially dehydrogenated) [23]. The exothermic peak at 431 °C (Fig. 7) was related to
33 the second dehydrogenation as confirmed by the DTG weight gain at 570 °C which is a
34 consequence of Fe^{2+} oxidation. The weak endothermic effect at 649 °C represents the total
35 dehydroxylation of crocidolite in good agreement with data reported by Hodgson et al. [20] in
36 which the total dehydroxylation of crocidolite was observed in the range of 570-700 °C. The broad
37 exothermic effect at 850 °C (Fig. 7) was related to the structure collapse and formation of
38 magnetite, cristobalite, and a pyroxene phase (acmite, $\text{NaFeSi}_2\text{O}_6$) [20].
39
40
41
42
43
44
45
46
47
48
49
50
51
52
53
54

55 At 928 °C, the DSC curve shows an endothermic peak due to the conversion of magnetite to
56 hematite. Indeed, in the DTG curve the peak at 928 °C stems from the oxidation of the ferrous iron
57
58
59
60
61
62
63
64
65

1 present in magnetite ($\text{Fe}^{+2}\text{Fe}^{+3}\text{O}_4$) which involves a weight gain (Fig. 7). The DSC shoulder effect
2 at 960 °C, which is clearly recorded on DDSC curve, was related to the incongruent melting point
3 of the acmite with separation of hematite [57, 58]. The endothermic peak observed at 1064 °C in the
4 DDSC curve indicated that cristobalite is being dissolved by the liquid [20]. Indeed, at 1100 °C the
5 final minerals products detected by PXRD were mainly hematite (33-0664 JCPDS card.) while
6 cristobalite (02-0278 JCPDS card) is evidently in a small amount because its reflections are close to
7 the detection limit (Fig. 8).
8
9

10
11
12
13
14
15
16
17 The structural changes of crocidolite with increasing temperature can be summarized in the
18 following steps: dehydrogenation and/or dehydroxylation accompanied by iron oxidation, structure
19 collapse and crystallization of newly formed crystalline phases, early melting. Crocidolite, blue at
20 room temperature, turned into dark red at 1100 °C, mostly due to hematite formation.
21
22
23
24
25

26 At SEM, the raw fibres of crocidolite appear as straight and rigid, looking like needles (Fig. 9a).
27 After heating at 1100 °C, the original morphology is strongly altered (Fig. 9b). The single fibres,
28 originally arranged in fibre bundles (Fig. 9a), now appear as thick sticks, confirming that partial
29 melting occurred during heating. However, it is still possible to recognize some fibrous-like
30 structure that was melt-bonded (Fig. 9b). At higher magnification (HM) crocidolite showed melt-
31 fragments composed of an aggregate of particles with totally different morphology with respect to
32 the original morphology (Fig. 9c).
33
34
35
36
37
38
39
40
41
42

43 *Tremolite*

44
45
46 DSC curve of tremolite asbestos from Val d'Ala (Fig. 10) exhibits a number of both endothermic
47 and exothermic peaks in the range 500-1100 °C that can be explained by the presence of impurities
48 in the sample [59]. The endothermic events at 729 °C and 776 °C are due to the dehydroxylation of
49 minor chlorite and antigorite, respectively [37, 36] (see Fig. 10 and Table 3). The exothermic peak
50 at 842 °C was related to oxidation of Fe^{2+} [60] present in the chlorite, its presence being also
51 proved by the weight gain in the DTG curve. The exothermic effect at 898 °C is interpreted as
52
53
54
55
56
57
58
59
60
61
62
63
64
65

1
2
3
4
5
6
7
8
9
10
11
12
13
14
15
16
17
18
19
20
21
22
23
24
25
26
27
28
29
30
31
32
33
34
35
36
37
38
39
40
41
42
43
44
45
46
47
48
49
50
51
52
53
54
55
56
57
58
59
60
61
62
63
64
65

recrystallization to forsterite and hematite. The shoulder at 955 °C on DSC curve was ascribed to talc breakdown [38], while the sharp endothermic peak at 1046 °C corresponds to breakdown of tremolite in agreement with Luckewicz [61]. The main TG weight loss of 2.02 % between 850 and 1050 °C due to the tremolite dehydroxylation (Fig. 10, Table 2) was in agreement with the theoretical tremolite water content [62]. Finally, the exothermic DSC signal at 1077 °C was related to the crystallization of diopside. The effect on TG curve (-0.17 wt%) below 110 °C was ascribed to the release of humidity adsorbed at the sample surface. The mineral products after heating to 1100 °C were diopside (JCPDS card 11-0654), forsterite and hematite deriving from tremolite and chlorite breakdown (Fig. 8).

Figure 9d depicts the typical morphology of tremolite fibres; they are stiff and exhibit a prismatic rod shaped morphology. After thermal treatment, the crystal habit is preserved but almost all the individuals result more brittle and fractured nearly perpendicular to the fibre axis (Fig. 9e). The HM Fig. 9f depicts the presence of newly-formed polyhedral crystals on the surface of the pristine tremolite asbestos some of which exhibit definite morphology with clear evidence of edges and faces. The growth occurs through the formation of recrystallizing-islands with heterogeneous lens shape. On the surface of the pristine tremolite asbestos the growth and coalescence of the recrystallizing-islands evolve from lens to faceted crystals. EDS/SEM investigations confirmed that the pseudomorphic process involves a complete recrystallization of the original tremolite asbestos into diopside.

Amosite

Characteristic DSC/TG thermogram of amosite is presented in Fig. 11. The first DSC weak peak at 288 °C is caused by the breakdown of goethite [63] present as impurity which transforms into hematite [64]. The second broad endothermic effect at 741 °C (Fig. 11) was related to the structural breakdown of amosite (Table 3), although amosite decomposition started at 600 °C with the formation of oxy-amosite [23, 26] and ended at about 850 °C in agreement with the literature data

1 [22, 23, 27]. Finally, the DSC curve shows a broad exothermic peak at 878 °C due to enstatite and
2 hematite formation, as confirmed by the PXRD pattern (Fig. 12). The very weak endothermic effect
3
4 in the range 530-580 °C (Fig. 11), evidenced in the DDSC curve, could be due to the structural
5
6 $\alpha \rightarrow \beta$ transition of quartz [65] which is present in the sample as impurity (Fig. 12).
7

8
9 The TG curve of amosite showed a continuous weight loss of 1.94 % between 110 and 690 °C, due
10
11 to dehydroxylation and dehydrogenation reactions [21, 26] which involve a weight gain of 0.24 %
12
13 between 690 and 1000 °C, due to oxidation of ferrous iron (Fig. 11). In fact, hematite (JCPDS card
14
15 24-0072) was also found among the final mineral products (Fig. 12) in addition to enstatite (JCPDS
16
17 card 07-0216) and quartz (JCPDS card 07-0346). The effect on TG curve (-0.33 wt%) below 110
18
19 °C was ascribed to the release of humidity adsorbed at the sample surface.
20
21
22

23
24 Raw amosite (Fig. 13a) shows fibres which look like flexible needle arranged in bundles. After
25
26 heating at 1100 °C, the newly-formed silicate (enstatite) preserved the original fibrous morphology
27
28 (pseudo-morphosis) but fibres appear more rigid and thicker (Fig. 13b). In some cases, single fibres
29
30 seem to be fused together at forming prismatic crystal (Fig. 13b, 13c) and when observed at higher
31
32 magnification, they appear partially covered by pseudo-spherical particles growing along the axial
33
34 direction of the fibres (Fig. 13c).
35
36
37

38 *Anthophyllite asbestos*

39
40
41 Figure 14 presents the thermal behaviour of anthophyllite asbestos. DTG curve shows one main
42
43 peak of maximum weight loss (2.30 %) at 868 °C due to anthophyllite dehydroxylation in
44
45 correspondence with the shoulder at 824 °C on DSC curve. However, DDSC confirm the presence
46
47 of an endothermic peak at 861 °C which corresponds to the structural breakdown of this phase [22,
48
49 27] followed by recrystallization of enstatite as showed by the exothermic peak at 915 °C (Fig. 14).
50
51 According to Freeman [27] the decomposition temperatures of anthophyllite asbestos as well as
52
53 tremolite asbestos were higher than those reported for amosite and crocidolite. The weak
54
55 endothermic peaks at 246 and 509 °C (Fig. 14) should be due to the dehydration and
56
57
58
59
60
61
62
63
64
65

1 dehydroxylation of vermiculite [66]. The DTG peaks at 972 and 1004 °C (Fig. 14) are interpreted as
2 the dehydroxylation of talc [38] and biotite [67] respectively, present as impurities. PXRD of
3 anthophyllite asbestos after heating to 1100 °C (Fig. 12) exhibits the lines of enstatite (02-0520
4 JCPDS card.) and cristobalite (03-0267 JCPDS card).

5
6
7
8
9
10
11
12
13
14
15
16
17
18
19
20
21
22
23
24
25
26
27
28
29
30
31
32
33
34
35
36
37
38
39
40
41
42
43
44
45
46
47
48
49
50
51
52
53
54
55
56
57
58
59
60
61
62
63
64
65
Fibres of anthophyllite asbestos appear straight, poorly flexible and thin and exhibit a slender
needle-like crystal habit both before and after heating treatment (Fig. 13d, 13e). SEM images
collected at higher magnification (Fig. 13f) showed that the new phase formed after heating
(enstatite) preserves the original fibre morphology (pseudomorphosis) but the surface becomes
rough.

Fibrous erionite

The TG curve of Fig. 15 showed a continuous weight loss due to the dehydration of erionite (H₂O
loss of 17.00 wt%), corresponding to the broad endothermic peak at 126 °C [29] and to the weak
endothermic peak at 356 °C (Table 3) on the DSC curve. In the first endothermic effect, the water
loss is 16.11 wt% while in the second endothermic the water loss is 0.89 wt%. The complete
dehydration is attained at 450 °C [68] without loss of crystallinity which started at temperature
above 700 °C (as verified by PXRD) followed by recrystallization of K-feldspars and plagioclase as
evidenced by the DSC exothermic peak at 911 °C (Fig. 15). The curves are in agreement with those
reported in Gottardi and Galli [69] and the estimated temperature of breakdown and
recrystallization is comparable to that (840 °C) reported by Ballirano and Cametti [70]. Differences
may be related not only to different experimental conditions but also to different Si/Al ratio, ionic
potential and size of exchangeable cations [19], and crystallite size of the various samples [70]. The
products of erionite recrystallization after heating to 1000 °C were K-feldspar, plagioclase and
quartz (see the PXRD in Fig. 16), according to the reaction sequence $\text{Na}_5\text{K}_3\text{Al}_8\text{Si}_{28}\text{O}_{72}\cdot 28\text{H}_2\text{O}$
(approximated erionite formula) $\rightarrow \text{Na}_5\text{K}_3\text{Al}_8\text{Si}_{28}\text{O}_{72} \rightarrow 3\text{KAlSi}_3\text{O}_8 + 5\text{NaAlSi}_3\text{O}_8 + 4\text{SiO}_2$.

1 At the SEM observation, erionite displays bundles composed of many fibres resembling amphibole
2 fibres morphology (stubby prismatic and acicular crystals) (Fig. 17a). After heating treatment the
3
4 new forms have feldspar-like composition as detected by EDS/SEM analyses. At low
5
6 magnification SEM, imaging show that the fibres are shorter but the original fibrous morphology is
7
8 preserved (Fig. 17b) and the surface is smooth. However, at higher magnification (Fig. 17c) the
9
10 surface of the fibrous crystals show irregularities and appear as rather rough (Fig. 17c).
11
12
13
14
15

16 **Conclusions**

17
18
19 Thermal decomposition of eight selected mineral fibres (chrysotile, four amphibole asbestos species
20
21 and erionite) has been investigated using DSC/TG supplemented by PXRD and SEM/EDS.
22
23

24 These investigations have shown that the decomposition of UICC chrysotile from Canada occurs at
25
26 633 °C while the structure breakdown for both chrysotile from Val Malenco and from Balangero
27
28 shift versus higher temperatures taking place at 652 °C and 660 °C respectively. The decomposition
29
30 of chrysotile is followed by the recrystallization into forsterite at about 822 °C. As it concerns
31
32 amphiboles, the breakdown of crocidolite, amosite, anthophyllite asbestos and tremolite asbestos
33
34 ranged from 850 to 1046 °C. Crocidolite asbestos UICC is decomposed at around 850 °C with the
35
36 formation of magnetite, cristobalite and acmite. However, at 1100 °C the final minerals products
37
38 were mainly hematite and partially melted cristobalite. Amosite UICC decomposes into enstatite
39
40 and hematite at 878 °C. Anthophyllite asbestos UICC breakdown leads to the formation of enstatite
41
42 and cristobalite at 861 °C. The breakdown of tremolite asbestos occurs at 1046 °C with the
43
44 consequent formation of diopside.
45
46
47
48
49

50 While for tremolite and anthophyllite asbestos the complete dehydroxylation occurs in one main
51
52 effect (1046 °C and 861 °C respectively) and leads to the breakdown of the mineral structure, the
53
54 dehydroxylation of amosite and crocidolite occurs in various steps in the temperature range 570 –
55
56 850 °C and it does not correspond with the structural collapse. Fibrous erionite shows the same
57
58
59
60
61
62
63
64
65

1
2
3
4
5
6
behaviour as that reported for amosite and crocidolite: although the complete dehydroxylation took
place between 25 and 425 °C, the loss of its crystallinity starts above 700 °C. The products of the
recrystallization after heating to 1000 °C are K-feldspar, albite and quartz.

7
8
9
10
The thermogravimetric (TG) analysis allowed the calculation of the water content in the fibres
which could be useful for the determination of their chemical formulae.

11
12
13
14
15
16
17
18
19
20
21
22
23
24
25
Despite the thermal treatment, all fibrous samples preserve the same external fibrous habit but the
structure is completely changed at a molecular scale: this phenomenon called pseudomorphosis lead
to the complete transformation of asbestos minerals into non-hazardous silicates such as forsterite
and enstatite. However, potentially hazardous minor phases such as cristobalite and quartz were
found in the new phases appeared after thermal treatment of anthophyllite asbestos, crocidolite and
asbestiform erionite; these may hinder a safe reuse of the processed asbestos samples.

26
27
28
29
30
31
32
33
34
35
36
37
38
39
40
Moreover, it has been demonstrated that DSC and DTG analyses are very effective for the
identification of minerals impurities both in chrysotile, amphibole asbestos and asbestiform erionite
specimens. Indeed, DSC and DTG analysis clearly showed the presence of low impurities, not
relievable by the semi-quantitative PXRD analysis, such as pyroaurite, talc, brucite, smectite,
dolomite, siderite, goethite, and biotite. However, all identified minerals are non-fibrous, mostly
having platy morphology.

41
42
43
44
45
46
47
48
49
50
51
52
53
54
55
56
The knowledge of the thermal behaviour of the eight fibrous samples studied in this work will allow
interpret thermograms obtained from natural samples and asbestos treated by heating with more
confidence.

57 58 59 60 61 62 63 64 65 **References**

- 1
2
3
4
5
6
7
8
9
10
11
12
13
14
15
16
17
18
19
20
21
22
23
24
25
26
27
28
29
30
31
32
33
34
35
36
37
38
39
40
41
42
43
44
45
46
47
48
49
50
51
52
53
54
55
56
57
58
59
60
61
62
63
64
65
1. Guthrie GD, Mossman BT. Merging the Geological and Biological Science an Integrated Approach to Mineral Induced Pulmonary Disease. In Guthrie GD, Mossman BT, editors. Health Effects of Mineral Dusts, Vol. 28, Reviews in Mineralogy & Geochemistry. Chelsea, MI: Mineralogical Soc. America Geochemical Soc; 1993. pp. 1–5.
2. Francine B, Ambrosi JP, Carbone M. Asbestos is not just asbestos: an unrecognised health hazard. *The lancet oncol.* 2013; 14.7: 576-8.
3. Whittaker EJW. The structure of chrysotile. V. Diffuse reflections and fibre texture. *Acta Crystallogr.* 1957;10:149–56.
4. Yada K. Study of microstructure of chrysotile asbestos by high-resolution electron microscopy. *Acta Crystallogr.* 1971;A 27:659–64.
5. Smith JV, Bennett JM. Enumeration of 4-connected 3-dimensional nets and classification of framework silicates; the infinite set of ABC-6 nets; the Archimedean and sigma-related nets. *Am Mineral.* 1981;66: 777-88.
6. Gualtieri G, Artioli E, Passaglia S, Bigi A, Viani JCH. Crystal structure-crystal chemistry relationships in the zeolites erionite and offretite, *Am Mineral.* 1998;83:590–606.
7. Gunter ME, Belluso E, Mottana A. Amphiboles: environmental and health concerns. In: Rosso JJ editor. *Reviews in Mineralogy and Geochemistry.* Chantilly, VA: Mineralogical Society of America Geochemical Society; 2007. pp. 453–516.
8. Kamp DW. Asbestos-induced lung diseases: an update. *Transl Res.* 2009;153:143–52.

- 1
2
3
4
5
6
7
8
9
10
11
12
13
14
15
16
17
18
19
20
21
22
23
24
25
26
27
28
29
30
31
32
33
34
35
36
37
38
39
40
41
42
43
44
45
46
47
48
49
50
51
52
53
54
55
56
57
58
59
60
61
62
63
64
65
9. Bertino P, Marconi A, Palumbo I, Bruni BM, Barbone D, Germano S, Dogan AU, Tassi GF, Porta C, Mutti I, Gaudino G. Erionite. Asbestos differently cause transformation of human mesothelial cells. *Int J Cancer*. 2007;121:2766–74.
 10. Plescia P, Gizzi D, Benedetti S, Camilucci L, Fanizza C, De Simone P, Paglietti F. Mechanochemical treatment to recycling asbestos-containing waste. *Waste Manage*. 2003;23:209–18.
 11. Favero-Longo SE, Castelli D, Fubini B, Piervittori R. Lichens on asbestos-cement roofs: Bioweathering and biocovering effects. *J Hazard Mater*. 2009;162:1300–8.
 12. Anastasiadou K, Axiotis D, Gidakos E. Hydrothermal conversion of chrysotile asbestos using near supercritical conditions. *J. Hazard. Mater*. 2010;179:926–32.
 13. Leonelli C, Veronesi P, Boccaccini DN, Rivasi MR, Barbieri L, Andreola F, Lancellotti I, Rabitti D, Pellacani GC. Microwave thermal inertisation of asbestos containing waste and its recycling in traditional ceramics. *J Hazard Mater*. 2006;135:149–55.
 14. Boccaccini DN, Leonelli C, Rivasi MR, Romagnoli M, Veronesi P, Pellacani GC, Boccaccini AR. Recycling of microwave inertised asbestos containing waste in refractory materials. *J Eur Ceram. Soc*. 2007;27:1855–8.
 15. Candela PA, Crummett CD, Earnest DJ, Frank MR, Wylie AG. Low-pressure decomposition of chrysotile as a function of time and temperature. *Am Mineral*. 2007;92:1704–13.
 16. Gualtieri AF, Cavenati C, Zanatto I, Meloni M, Elmi G, Lassinantti Gualtieri M. The transformation sequence of cement–asbestos slates up to 1200°C and safe recycling of the reaction product in stoneware tile mixtures. *J Hazard Mater*. 2008;152:563–70.

- 1
2
3
4
5
6
7
8
9
10
11
12
13
14
15
16
17
18
19
20
21
22
23
24
25
26
27
28
29
30
31
32
33
34
35
36
37
38
39
40
41
42
43
44
45
46
47
48
49
50
51
52
53
54
55
56
57
58
59
60
61
62
63
64
65
17. Dellisanti F, Rossi PL, Valdre` G. Remediation of Asbestos Containing Materials by Joule heating vitrification performed in a pre-pilot apparatus. *Int J Miner Process.* 2009;91:61–7.
 18. Yvon Y, Sharrock P. Characterization of thermochemical inactivation of Asbestos Containing Wastes and recycling the mineral residues in cement products. *Waste Biomass Valor.* 2011;2:169–81.
 19. Cattaneo A, Gualtieri AF, Artioli G. Kinetic study of the dehydroxylation of chrysotile asbestos with temperature by in situ XRPD. *Phys Chem Miner.* 2003;30:177-83.
 20. Hodgson AA, Freeman AG, Taylor HFW. The thermal decomposition of crocidolite from Koegas, South Africa. *Miner Mag.* 1965;35:5–30.
 21. Rouxhet PG, Gillard JL, Fripiat JJ. Thermal decomposition of amosite, crocidolite, and biotite. *Mineral Mag.* 1972;38:583-92.
 22. Kohyama N, Shinohama Y, Suzuki Y. Mineral phases and some re-examined characteristics of the International Union Against Cancer standard asbestos samples. *Am J Ind Med.* 1996;30:515-28.
 23. Jeyaratnam M, West NG. A study of heat-degraded chrysotile, amosite and crocidolite by X-ray diffraction, *Ann Occup Hyg.* 1994;38:137–48.
 24. Gualtieri AF, Levy D, Belluso E, Dapiaggi M. Kinetics of the decomposition of crocidolite asbestos: a preliminary real-time X-ray powder diffraction study. *Miner Sci Forum.* 2004;443–444: 291–4.

- 1
2
3
4
5
6
7
8
9
10
11
12
13
14
15
16
17
18
19
20
21
22
23
24
25
26
27
28
29
30
31
32
33
34
35
36
37
38
39
40
41
42
43
44
45
46
47
48
49
50
51
52
53
54
55
56
57
58
59
60
61
62
63
64
65
25. Kusiorowski R, Zaremba T, Gerle A, Piotrowski J, Simka W, Adamek J. Study on the thermal decomposition of crocidolite asbestos. *J Therm Anal Calorim.* 2015. doi: 10.1007/s10973-015-4421-7.
26. Hodgson AA, Freeman AG, Taylor HFW. The thermal decomposition of amosite. *Miner Mag.* 1965;35:445–63.
27. Freeman AG. The dehydroxylation behavior of amphibole. *Miner Mag.* 1966;35:953–7.
28. Kusiorowski R, Zaremba T, Piotrowski J, Adamek J. Thermal decomposition of different types of asbestos. *J Therm Anal Calorim.* 2012;109: 693-704.
29. Papke, KG. Erionite and associated zeolites in Nevada. *Nev Bur Mines Geol Bull.* 1972;79:1-31.
30. Pugnali A, Giantomassi F, Lucarini G, Capella S, Bloise A, Di Primio R, Belluso E. (2013) Cytotoxicity induced by exposure to natural and synthetic tremolite asbestos: an in vitro pilot study. *Acta Histochem.* 2013;115:100–12.
31. Duncan KE, Cook PM, Gavett SH, Dailey LA, Mahoney RK, Ghio AJ, Roggli VL, Devlin RB. In vitro determinants of asbestos fiber toxicity: Effect on the relative toxicity of Libby amphibole in primary human airway epithelial cells. *Part Fibre Toxicol.* 2014;11:1-14.
32. Pollastri S, Gualtieri AF, Lassinantti Gualtieri M, Hanuskova M, Cavallo A, Gaudino G. The zeta potential of mineral fibres. *J Hazard Mater.* 2014; 276:469–79.
33. Frost RL, Erickson KL. Thermal decomposition of synthetic hydrotalcites reevesite and pyroaurite. *J Therm Anal Calorim.* 2004;76: 217-25.

- 1
2 34. Kissinger HE. Reaction kinetics in differential thermal analysis. *Anal Chem.* 1957;29:1702-6.
3
4
5
6
7 35. Gallagher PK, Warne SStJ. Thermomagnetometry and thermal decomposition of siderite.
8
9 *Thermochim Acta.* 1981;43: 253-67.
10
11
12
13 36. Viti C. Serpentine minerals discrimination by thermal analysis. *Am Mineral.* 2010;95:631–8.
14
15
16
17
18 37. Villieras F, Yvon J, Cases JM, De Donato P, Lhote F, Baeza R. Development of microporosity
19
20 in clinocllore upon heating. *Clay Clay Miner.* 1994;42: 679-88.
21
22
23
24
25 38. Catalano M, Belluso E. Miriello D, Barrese E, Bloise A. Synthesis of Zn-doped talc in
26
27 hydrothermal atmosphere. *Cryst Res Technol.* 2014;49:283–9, 2014.
28
29
30
31 39. Ball MC, Taylor HFW. The dehydration of chrysotile in air and under hydrothermal conditions.
32
33 *Mineral Mag.* 196;33:467–82.
34
35
36
37
38 40. Brindley GW, Hayami R. Mechanism of formation of forsterite and enstatite from serpentine.
39
40 *Mineral Mag.* 1965;35:189–95.
41
42
43
44 41. Martin CJ. The thermal decomposition of chrysotile. *Mineral Mag.* 1977;41:453–9.
45
46
47
48
49 42. MacKenzie KJD, Meinhold RH. Thermal reactions of chrysotile re–vised: A ²⁹Si and ²⁵Mg
50
51 MAS NMR study. *Am Mineral.* 1994;79:43–50.
52
53
54
55 43. Bloise A, Belluso E, Barrese E, Miriello D, Apollaro C. Synthesis of Fe-doped chrysotile and
56
57 characterization of the resulting chrysotile fibers. *Cryst Res Technol.* 2009;44:590-6.
58
59
60
61
62
63
64
65

- 1
2 44. Bloise A, Belluso E, Fornero E, Rinaudo C, Barrese E, Capella S. Influence of synthesis
3 conditions on growth of Ni-doped chrysotile. *Micropor Mesopor Mat.* 2010;132:239-45.
4
5
6
7
8
9 45. Gunasekaran S, Anbalagan G. Thermal decomposition of natural dolomite. *B Mater Sci.*
10 2007;30:339-44.
11
12
13
14
15 46. Bloise A, Critelli T, Catalano M, Apollaro C, Miriello D, Croce A, Barrese E, Liberi F, Piluso
16 E, Rinaudo C, Belluso E. Asbestos and other fibrous minerals contained in the serpentinites of the
17 Gimigliano-Mount Reventino Unit (Calabria, S-Italy). *Environ Earth Sci.* 2014;71:3773-86.
18
19
20
21
22
23 47. Viti C, Giacobbe C, Gualtieri AF. Quantitative determination in massive serpentinites using
24 DTA: implications for asbestos determination, *Am Miner.* 2011;96:1003–11.
25
26
27
28
29
30 48. Cattaneo A, Somigliana A, Gemmi M, Bernabeo F, Savoca D, Cavallo DM, Bertazzi PA.
31 Airborne Concentrations of Chrysotile Asbestos in Serpentine Quarries and Stone Processing
32 Facilities in Valmalenco, Italy. *Ann Occup Hyg.* 2012; 1–13.
33
34
35
36
37
38 49. Lesci IG, Balducci G, Pierini F, Soavi F, Roveri N. Surface features and thermal stability of
39 mesoporous Fe doped geoinspired synthetic chrysotile nanotubes. *Micropor Mesopor Mat.*
40 2014;197:8-16.
41
42
43
44
45
46 50. Lafay R, Montes-Hernandez G, Janots E, Auzende AL, Chiriac R, Lemarchand D, Toche F.
47 Influence of trace elements on the textural properties of synthetic chrysotile: Complementary
48 insights from macroscopic and nanoscopic measurements. *Micropor Mesopor Mat.* 2014;183:81–
49 90.
50
51
52
53
54
55
56
57
58
59
60
61
62
63
64
65

- 1
2
3
4
5
6
7
8
9
10
11
12
13
14
15
16
17
18
19
20
21
22
23
24
25
26
27
28
29
30
31
32
33
34
35
36
37
38
39
40
41
42
43
44
45
46
47
48
49
50
51
52
53
54
55
56
57
58
59
60
61
62
63
64
65
51. Wypych F, Schreiner WH, Mattoso N, Mosca DH, Marangonia R, Bento CAS. Covalent grafting of phenylphosphonate groups onto layered silica derived from in situ-leached chrysotile fibers. *J Mater Chem*. 2003;13:304-7.
52. Giacobbe C, Gualtieri AF, Quartieri S, Rinaudo C, Allegrina M, Andreozzi GB. Spectroscopic study of the product of thermal transformation on Chrysotile-Asbestos Containing Materials. *Eur J Mineral*. 2010;22:535–46.
53. Croce A, Allegrina M, Trivero P, Rinaudo C, Viani A, Pollastri S, Gualtieri AF. The concept of ‘end of waste’ and recycling of hazardous materials: in depth characterization of the product of thermal transformation of cement-asbestos. *Mineral Mag*. 2014;78:1177-91.
54. Fujishige M, Kuribara A, Karasawa I, Kojima A. Low-temperature pyrolysis of crocidolite and amosite using calcium salts as a flux. *J Ceram Soc Jpn*. 2007;115:434-9.
55. Addison CC, Addison WE, Neal GA, Sftarv JH. Amphiboles Part I: The oxidation of crocidolite. *Journ Chem Soc*. 1962;278:1468-71.
56. Brindley GW, Youell RF. Ferrous chamosite and ferric chamosite. *Min Mag*. 1953;30:57-70.
57. Yagi K. The system acmite-diopside and its bearing on the stability relations of natural pyroxenes of the acmite–hedenbergite–diopside series. *Am Mineral*. 1966;51:976–1000.
58. Bowen NL, Schairer JF. The fusion relations of acmite. *Amer J Sci ser 5*. 1929;18:365-74.
59. MacKenzie RC. The differential thermal investigation of clays. London: Mineralogical Society (Clay Minerals Group); 1957.
60. Jones AA. Charges on the surfaces of two chlorites. *Clay Miner*. 1981;16:347-59.

1
2
3
4
5
6
7
8
9
10
11
12
13
14
15
16
17
18
19
20
21
22
23
24
25
26
27
28
29
30
31
32
33
34
35
36
37
38
39
40
41
42
43
44
45
46
47
48
49
50
51
52
53
54
55
56
57
58
59
60
61
62
63
64
65

61. Luckewicz W. Differential thermal analysis of chrysotile asbestos in pure talc and talc containing other minerals. *J Soc Cosmet Chem.* 1975;26:431-437.

62. Bloise A, Fornero E, Belluso E, Barrese E, Rinaudo C. Synthesis and characterization of tremolite asbestos fibres. *Eur J Mineral.* 2008;20:1027-33.

63. Gualtieri AF, Venturelli P. In situ study of the goethite-hematite phase transformation by real time synchrotron powder diffraction. *Am Mineral.* 1999;84:895–904.

64. Miriello D, Bloise A, De Francesco A, Crisci GM, Chiaravalloti F, Barca D, La Russa MF, Marasco E. Colour and composition of nodules from the Calabrian clay deposits: a possible raw material for pigments production in Magna Graecia. *Period Mineral.* 2010;79:59-69.

65. Moore GSM, Rose HE. The structure of powdered quartz. *Nature.* 1973;242:187–90.

66. Brydon JE, Turner RC. The nature of Kenya vermiculite and its aluminum hydroxide complexes. *Clays Clay Miner.* 1972;20:1-11.

67. Bagin VI, Gendler TS, Dainyak LG, Kuz'min RN. Mossbauer, thermomagnetic, and x-ray study of cation ordering and high-temperature decomposition in biotite. *Clays Clay Miner.* 1980;28:188-96.

68. Ballirano P, Andreozzi GB, Dogan M, Dogan AU. Crystal structure and iron topochemistry of erionite-K from Rome, Oregon, U.S.A. *Am Mineral.* 2009;94:1262-70.

69. Gottardi G, Galli E. *Natural zeolites.* Berlin: Springer-Verlag; 1985.

70. Ballirano P, Cametti G. Dehydration dynamics and thermal stability of erionite-K:
Experimental evidence of the “internal ionic exchange” mechanism. *Micropor Mesopor Mat.*
2012;163:160-8.

1
2
3
4
5
6
7
8
9
10
11
12
13
14
15
16
17
18
19
20
21
22
23
24
25
26
27
28
29
30
31
32
33
34
35
36
37
38
39
40
41
42
43
44
45
46
47
48
49
50
51
52
53
54
55
56
57
58
59
60
61
62
63
64
65

Sample	Calculated chemical formula	Provenance
Chrysotile UICC	$(Mg_{5.93}Fe^{2+}_{0.04}Al_{0.02}Fe^{3+}_{0.08})_6.07Si_{4.03}O_{10}(OH)_{7.66}$	Quebec (Canada) ^{a*}
Chr Balangero	$(Mg_{5.81}Fe^{2+}_{0.15}Al_{0.27}Fe^{3+}_{0.09}Cr_{0.01})_6.33Si_{3.97}O_{10}(OH)_{7.11}$	Val Malenco, Sondrio (Italy)
Chr Val Malenco	$(Mg_{5.85}Fe^{2+}_{0.06}Al_{0.02}Fe^{3+}_{0.05}Ni_{0.01})_5.99Si_{4.01}O_{10}(OH)_{7.86}$	Balangero, Turin (Italy)
Amosite	$(Ca_{0.02}Na_{0.01})(Fe^{2+}_{5.36}Mg_{1.48}Fe^{3+}_{0.11}Mn_{0.06})_7.01(Si_{7.93}Al_{0.01})_7.94O_{21.94}(OH)_{2.06}$	Penge mine, Northern Province (South Africa) [§]
Anthophyllite	$Ca_{0.04}(Mg_{5.81}Fe^{2+}_{0.92}Fe^{3+}_{0.21}Mn_{0.04})_6.98(Si_{7.83}Al_{0.02})_7.83O_{21.63}(OH)_{2.37}$	Paakkila mine, Paakkila (Finland) [†]
Crocidolite	$(Na_{1.96}Ca_{0.03}K_{0.01})_2(Fe^{2+}_{2.34}Fe^{3+}_{2.05}Mg_{0.52})_4.91(Si_{7.84}Al_{0.02})_7.86O_{21.36}(OH)_{2.64}$	Koegas Mine, Northern Cape (South Africa) [#]
Tremolite	$(Ca_{1.91}Na_{0.06}K_{0.01})_{1.98}(Mg_{4.71}Fe^{2+}_{0.22}Fe^{3+}_{0.08}Mn_{0.02})_5.03(Si_{8.01}Al_{0.02})_8.03O_{22.14}(OH)_{1.86}$	Val d'Ala, Turin (Italy)
Erionite	$(Na_{5.35}K_{2.19}Ca_{0.15}Mg_{0.11}Ti_{0.05})_7.85(Si_{28.01}Al_{7.90})_{35.91}O_{72} \cdot 28.13H_2O$	Jersey, Nevada (USA)

Table 1 Calculated chemical formulae (After Pollastri et al., 2015 [38]) and details of the investigated minerals fibres.

^aMixture of fiber from the firms Bells, Carey, Cassair, Flintkote, Johns-Manville, Lake, Normandie and National, proportioned roughly to represent Canadian production of asbestos products at that time. *UICC standard Chrysotile “B” Canadian NB #4173-111-1; [§]UICC standard Amosite from Penge mine South African; [†]UICC standard Anthophyllite Finnish NB #4173-111-5; [#]UICC standard Crocidolite South African NB #4173-111-3

Chrysotile from Canada UICC		Chrysotile from Balangero		Chrysotile from Val Malenco	
T range (°C)	TG loss %	T range (°C)	TG loss %	T range (°C)	TG loss %
25-110	0.91	25-110	0.57	25-110	0.54
430-800	12.22	430-800	11.80	430-800	12.01
tot loss at 1000	18.66	tot loss at 1000	14.87	tot loss at 1000	13.35
Crocidolite from S. Africa UICC		Tremolite from Val d'Ala		Amosite from Penge UICC	
T range (°C)	TG loss %	T range (°C)	TG loss %	T range (°C)	TG loss %
25-110	0.58	30-110	0.17	25-110	0.33
110-680	2.18	850-1100	2.02	110-690	1.94
tot loss at 1100	2.76	tot loss at 1100	3.43	tot loss at 1100	2.17
Anthophyllite from Paakkila UICC		Erionite from Nevada			
T range (°C)	TG loss %	T range (°C)	TG loss %		
25-110	0.11				
110-690	2.30	25-450	17.00		
tot loss at 1100	4.98	tot loss at 1000	17.99		

Table 2 Main TG data (weight loss %)

1
2
3
4
5
6
7
8
9
10
11
12
13
14
15
16
17
18
19
20
21
22
23
24
25
26
27
28
29
30
31
32
33
34
35
36
37
38
39
40
41
42
43
44
45
46
47
48
49
50
51
52
53
54
55
56
57
58
59
60
61
62
63
64
65

DSC T (°C)	Chrysotile from Canada UICC	Chrysotile from Balangero	Chrysotile from Val Malenco	Crocidolite from S. Africa UICC	Tremolite from Val d'Ala	Amosite from Penge UICC	Anthophyllite from Paakkila UICC	Erionite from Nevada
226	endo w			320	exo w	288	endo	246 endo w 126 endo s
401	endo w	402	endo	354	endo w			356 endo w
520	endo w		557	endo w	431	exo w	535	sh 509 endo w
633	endo s	660	endo s	652	endo s	649	endo w	729 endo s 741 endo w 824 sh
				850	exo			
823	exo s	822	exo s	820	exo s	928	endo s	776 endo w 878 exo 915 exo s 911 exo
				960	sh	842	exo w	
						898	exo w	
						955	sh	
				1064	sh	1046	endo s	
						1077	exo	

Table 3 Peak temperatures in DSC curves; w = weak, s = strong, sh = shoulder, endo= endothermic, exo = exothermic

1
2
3
4
5
6
7
8
9
10
11
12
13
14
15
16
17
18
19
20
21
22
23
24
25
26
27
28
29
30
31
32
33
34
35
36
37
38
39
40
41
42
43
44
45
46
47
48
49
50
51
52
53
54
55
56
57
58
59
60
61
62
63
64
65

Figure captions

Fig. 1 Thermal analysis of chrysotile UICC from Canada. Solid line: DSC. Dashed line: DTG. Dotted line: TG

Fig. 2 PXRD patterns recorded before (b) and after (a) heating at 1000 °C for the three kinds of chrysotile; from the bottom to top chrysotile UICC (CCb and CCa); chrysotile from Balangero (CBb and CBa); chrysotile from Val Malenco (CVMb and CVMa)

Fig. 3 Thermal analysis of chrysotile from Balangero. Solid line: DSC. Dashed line: DTG. Dotted line: TG

Fig. 4 Thermal analysis of chrysotile from Val Malenco. Solid line: DSC. Dashed line: DTG. Dotted line: TG

Fig. 5 Comparison of DSC curves recorded for chrysotile from Balangero (CB), from Val Malenco (CVM) and UICC from Canada (CC)

Fig. 6 Secondary electron SEM images of the three kinds of chrysotile: UICC from Canada, first line; from Balangero, second line; from Val Malenco, third line. From left to right: first column (a, d, g), before heating treatment at 1000 °C; second and third column (b, c, e, f, h, i), after heating. Images c, f, i acquired with high resolution SEM, testifying the pseudomorphic transformation of the chrysotile fibres with temperature

Fig. 7 Thermal analysis of crocidolite UICC. Solid line: DSC. Dashed line: DTG. Dotted line: TG

Fig. 8 PXRD patterns recorded before b and after a heating at 1000 °C of crocidolite UICC (Crb and Cra); tremolite asbestos (Tb and Ta)

Fig. 9 Secondary electron SEM images of crocidolite UICC (first line) and tremolite asbestos (second line). From left to right: first column (a, d), before heating treatment at 1000 °C; second and third column (b, e, c, f), after heating. Images c, i acquired with high resolution SEM, showing a complete pseudo-morphic recrystallization occurred to fibres. Arrow in b indicates crocidolite fibres partially melted

1
2
3
4
5
6
7
8
9
10
11
12
13
14
15
16
17
18
19
20
21
22
23
24
25
26
27
28
29
30
31
32
33
34
35
36
37
38
39
40
41
42
43
44
45
46
47
48
49
50
51
52
53
54
55
56
57
58
59
60
61
62
63
64
65

Fig. 10 Thermal analysis of tremolite asbestos from Val d'Ala. Solid line: DSC. Dashed line: DTG. Dotted line: TG

Fig. 11 Thermal analysis of amosite. Solid line: DSC. Dashed line: DTG. Dotted line: TG

Fig. 12 PXRD patterns recorded before **b** and after **a** heating at 1000 °C of anthophyllite asbestos UICC (Anb and Ana)

Fig.13 Secondary electron SEM images of amosite (first line) and anthophyllite asbestos UICC (second line). From left to right: first column (**a, d**), before heating treatment at 1000 °C; second and third column (**b, e, c, f**), after heating. High resolution SEM images **c** and **i** show the fibrous recrystallized forms

Fig. 14 Thermal analysis of anthophyllite asbestos UICC. Solid line: DSC. Dashed line: DTG. Dotted line: TG

Fig. 15 Thermal analysis of asbestiform erionite. Solid line: DSC. Dashed line: DTG. Dotted line: TG

Fig. 16 PXRD patterns from asbestiform erionite before (Erb) and after (Era) heating at 1000 °C

Fig.17 Secondary electron SEM images of asbestiform erionite **a** before and **b, c** after; heating treatment at 1000 High resolution SEM Image **c** shows rough surface

Fig.1

[Click here to download Figure: Fig. 1.tif](#)

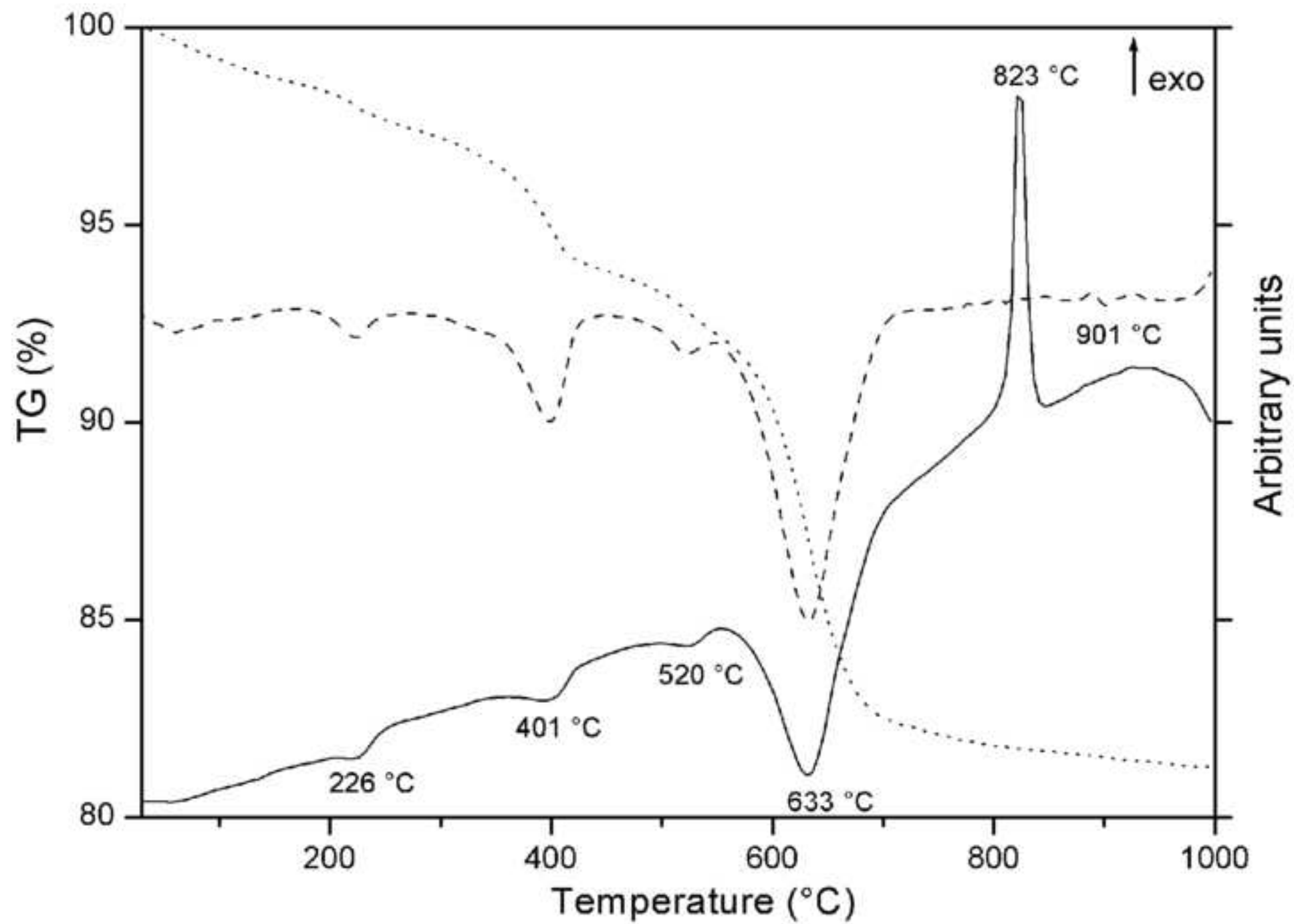


Fig.2
[Click here to download Figure: Fig. 2.tif](#)

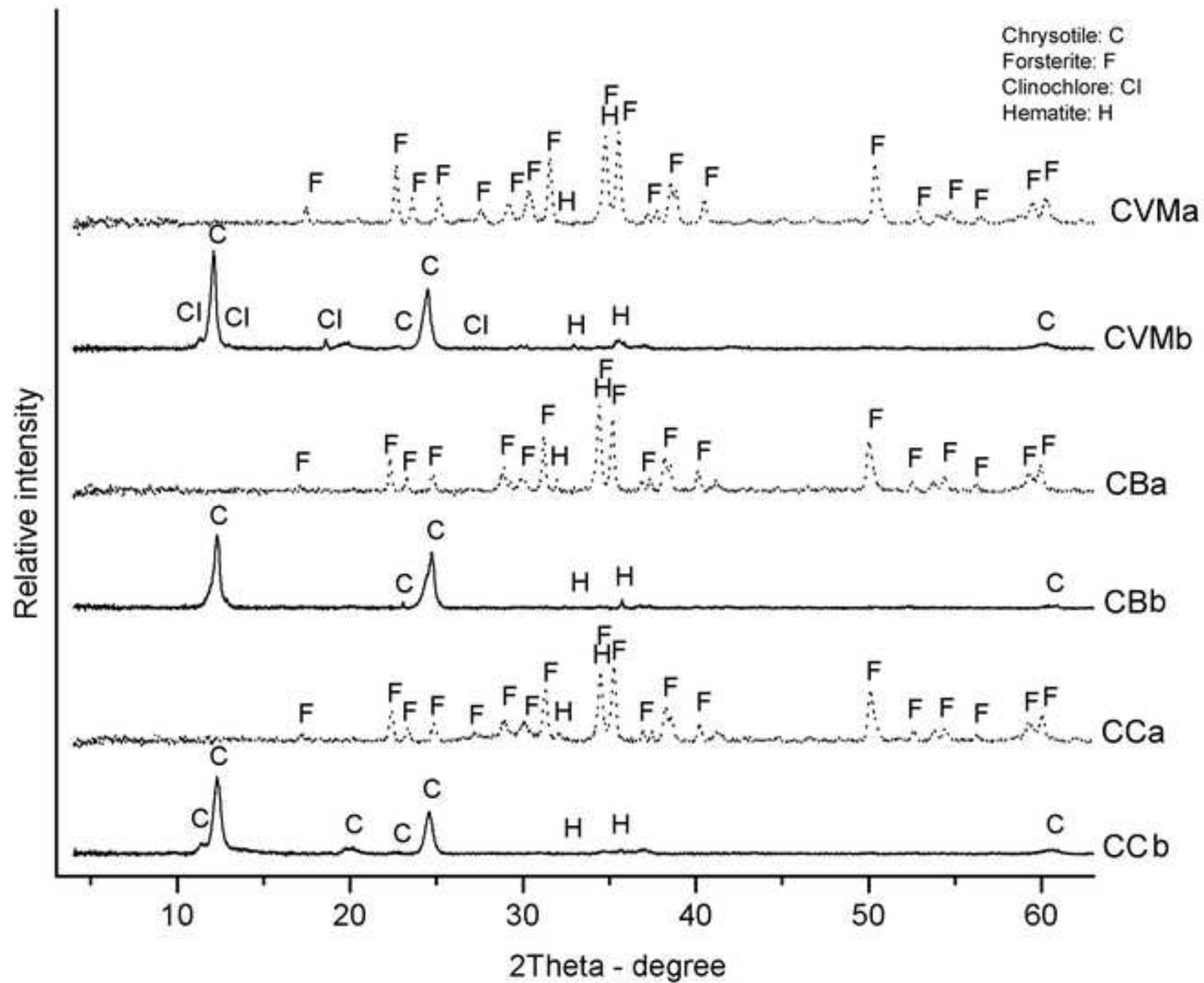


Fig.3

[Click here to download Figure: Fig. 3.tif](#)

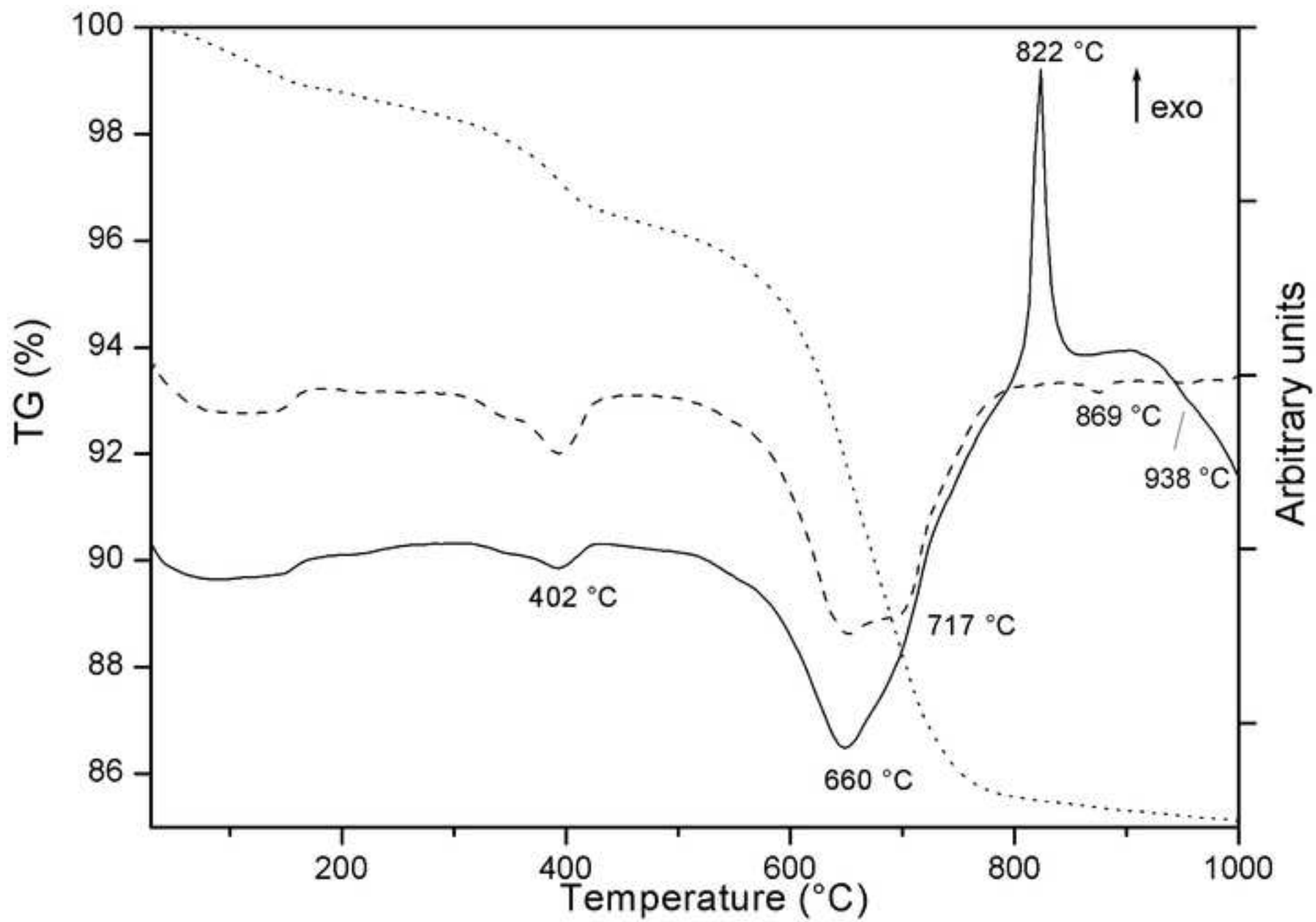


Fig.4

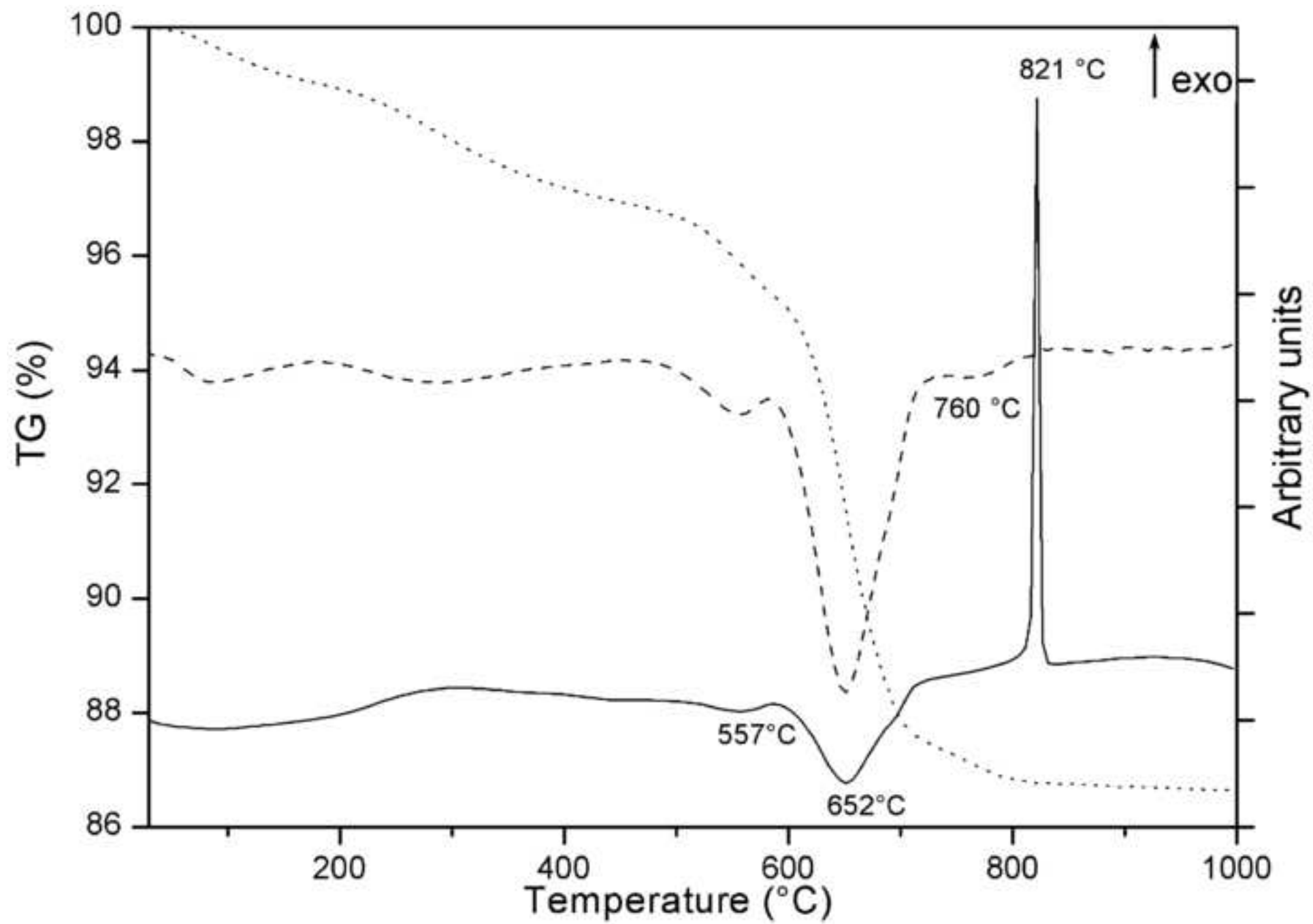
[Click here to download Figure: Fig. 4.tif](#)

Fig.5
[Click here to download Figure: Fig. 5.tif](#)

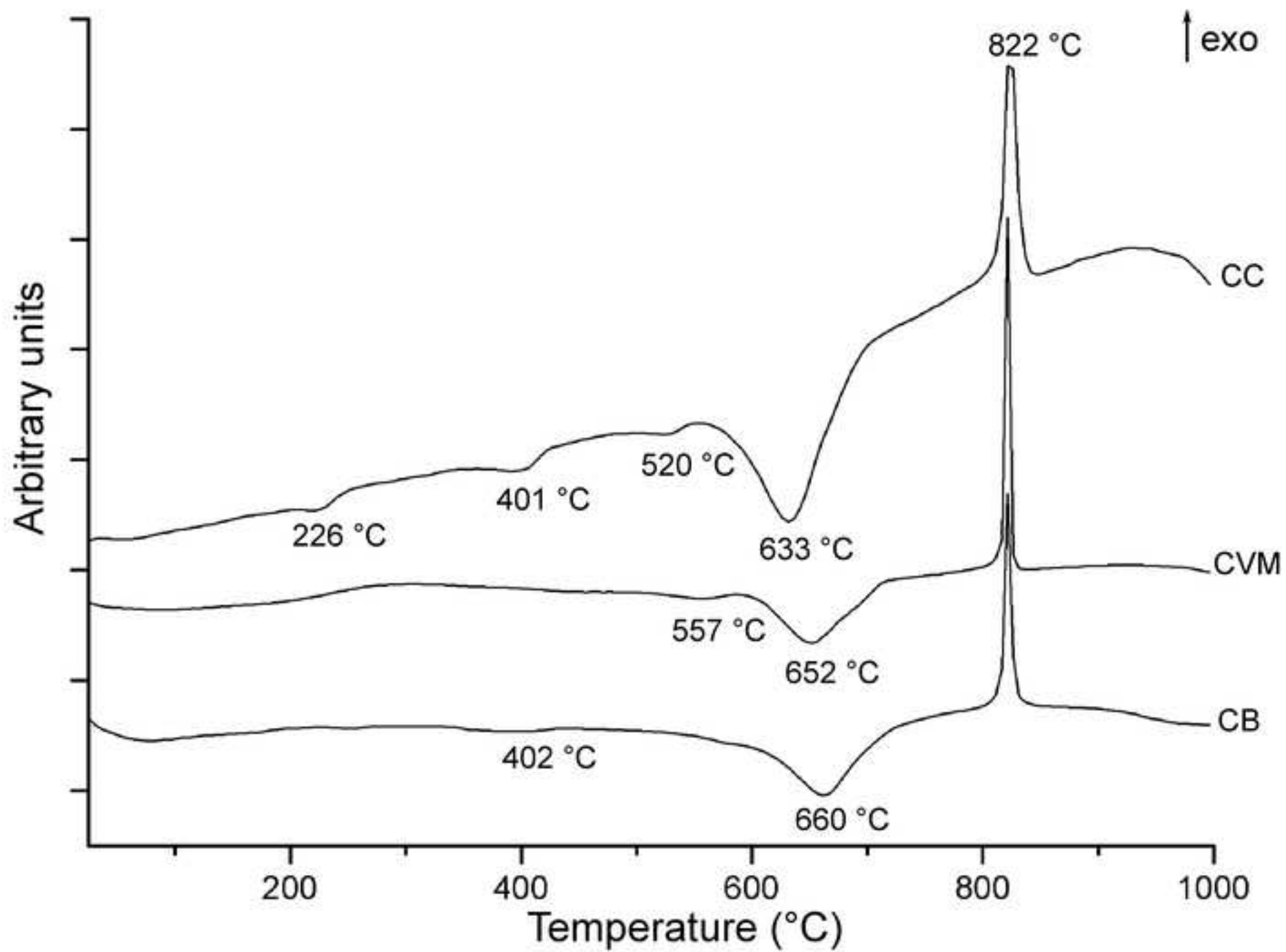


Fig.6

[Click here to download Figure: Fig. 6.tif](#)

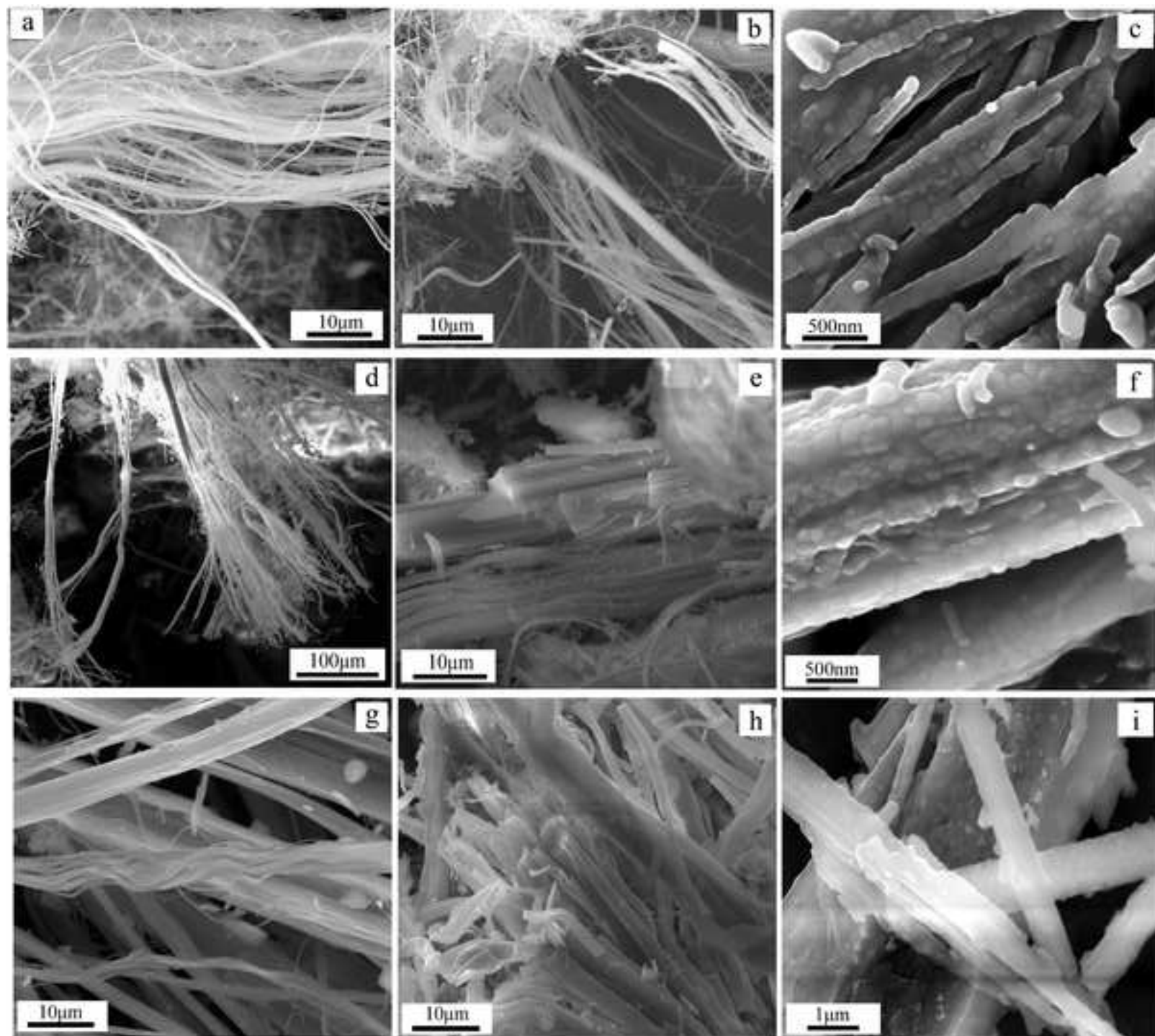


Fig.7

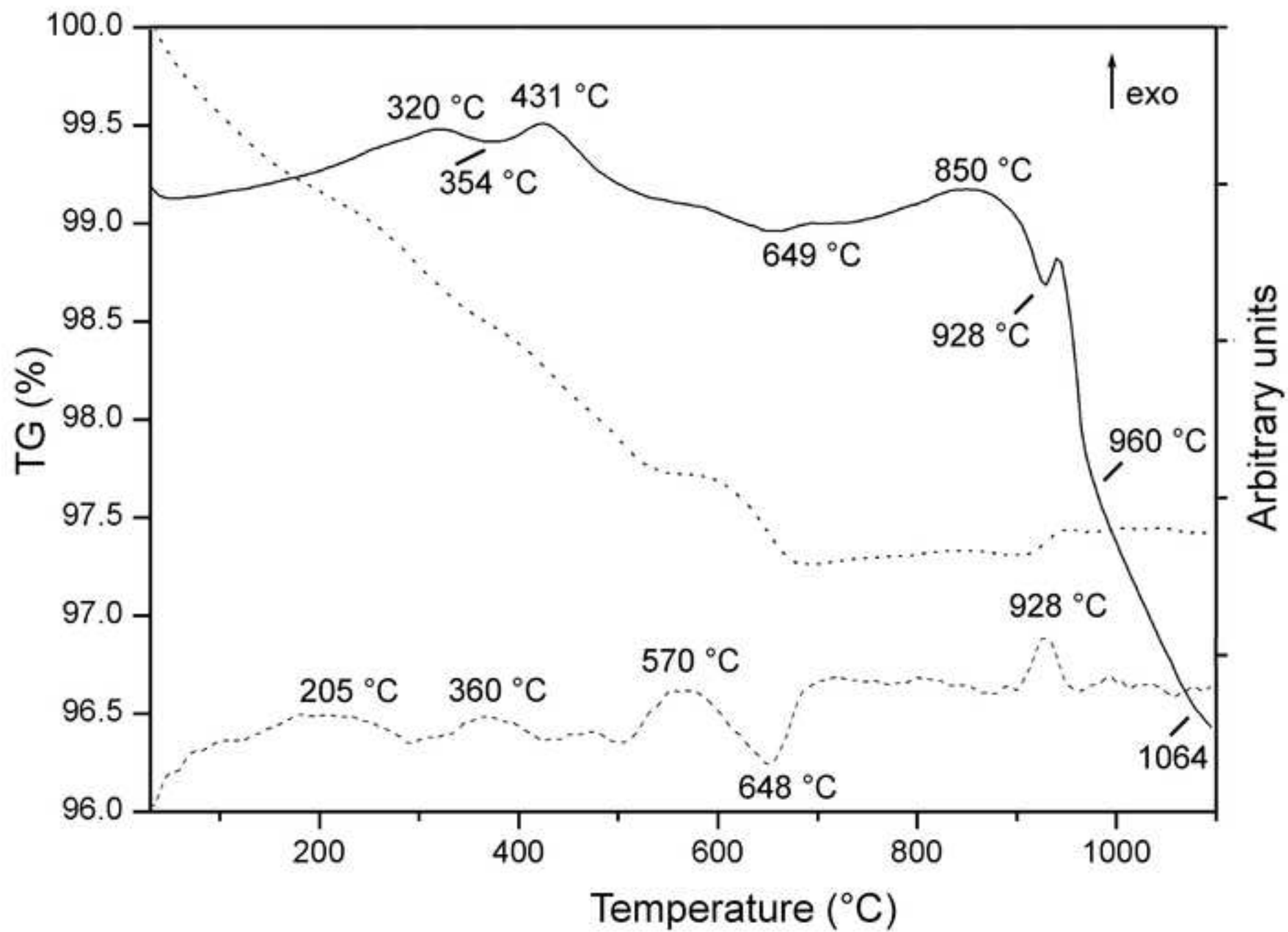
[Click here to download Figure: Fig. 7.tif](#)

Fig.8
[Click here to download Figure: Fig. 8.tif](#)

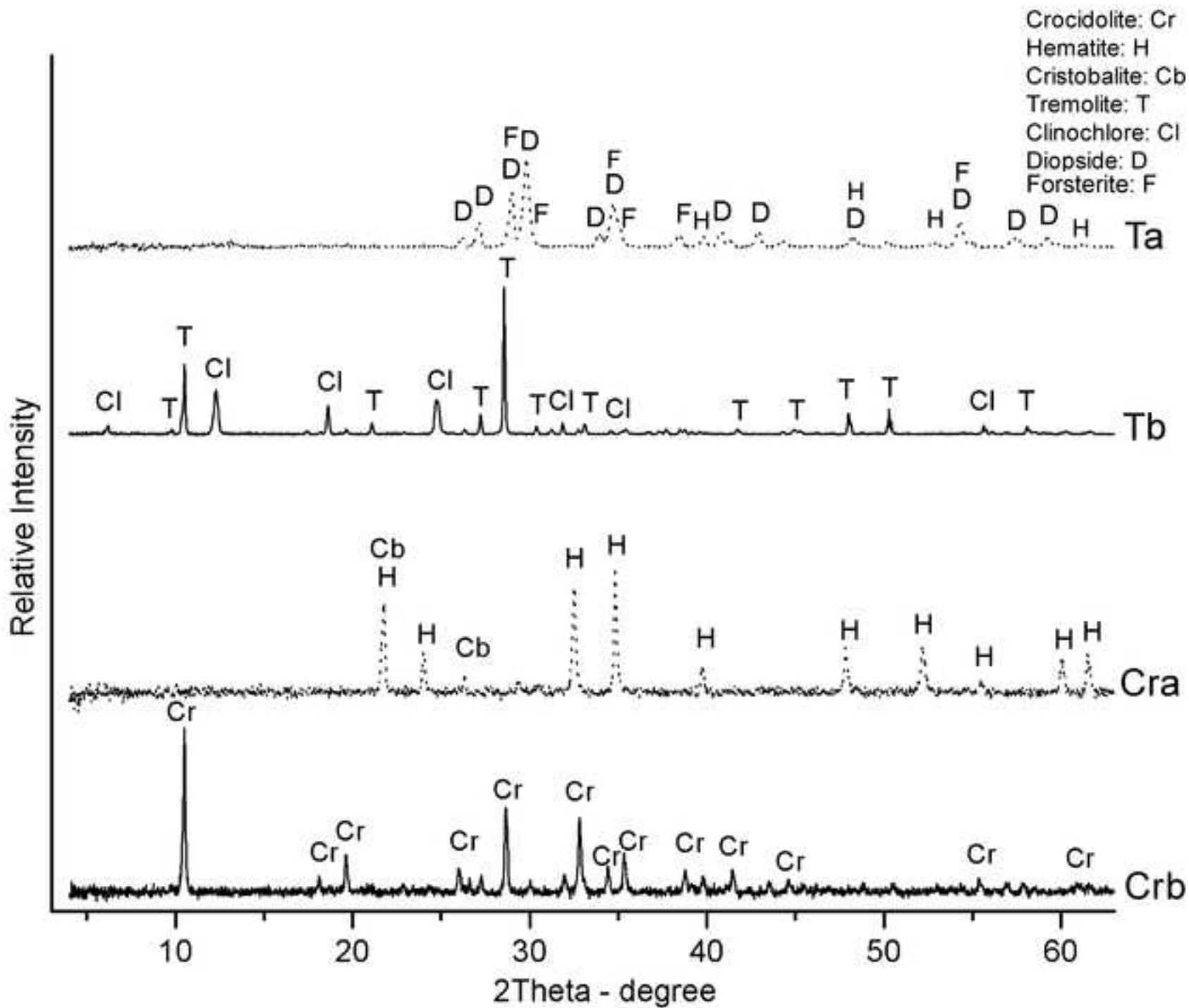


Fig.9

[Click here to download Figure: Fig. 9.tif](#)

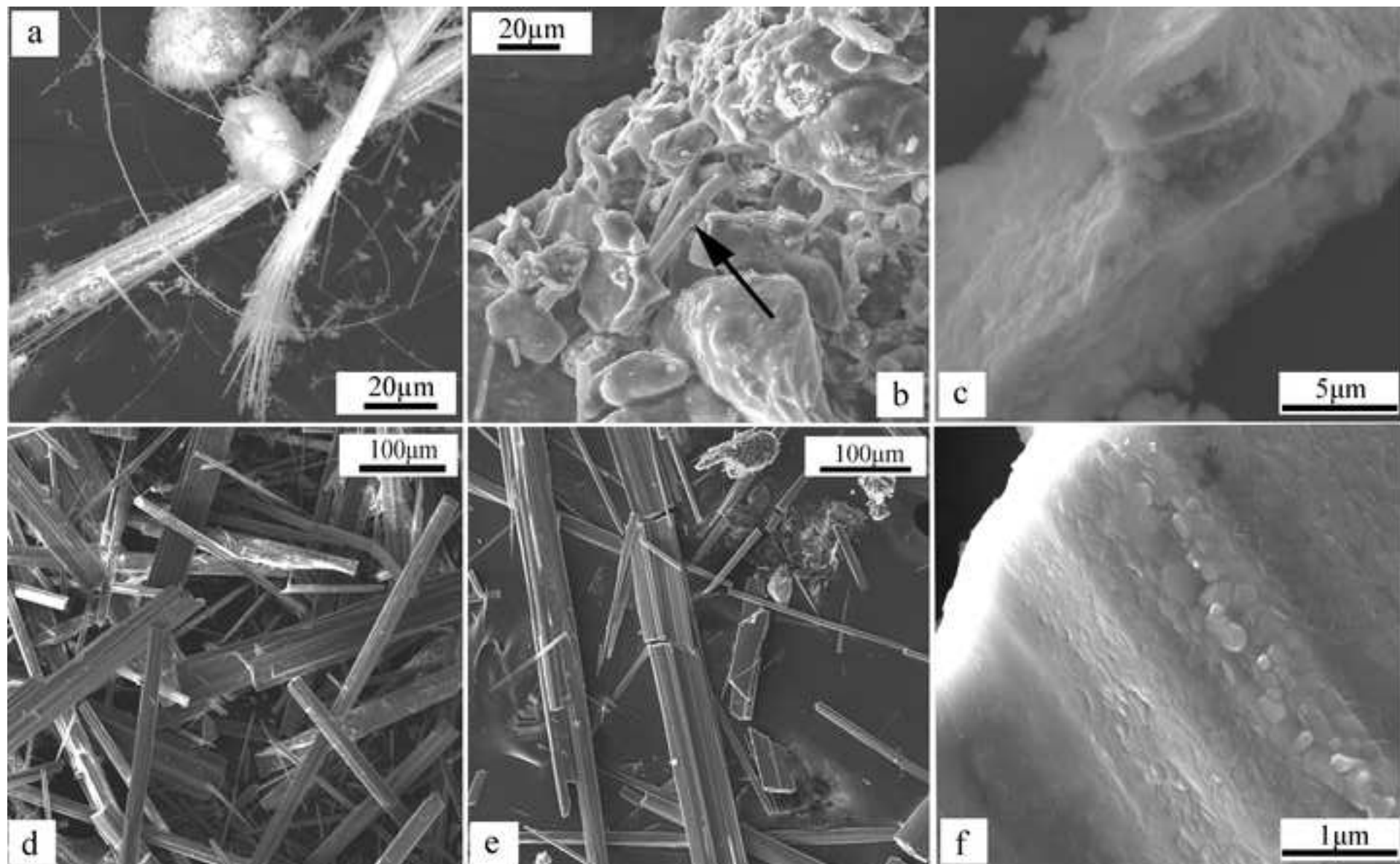


Fig.10

[Click here to download Figure: Fig. 10.tif](#)

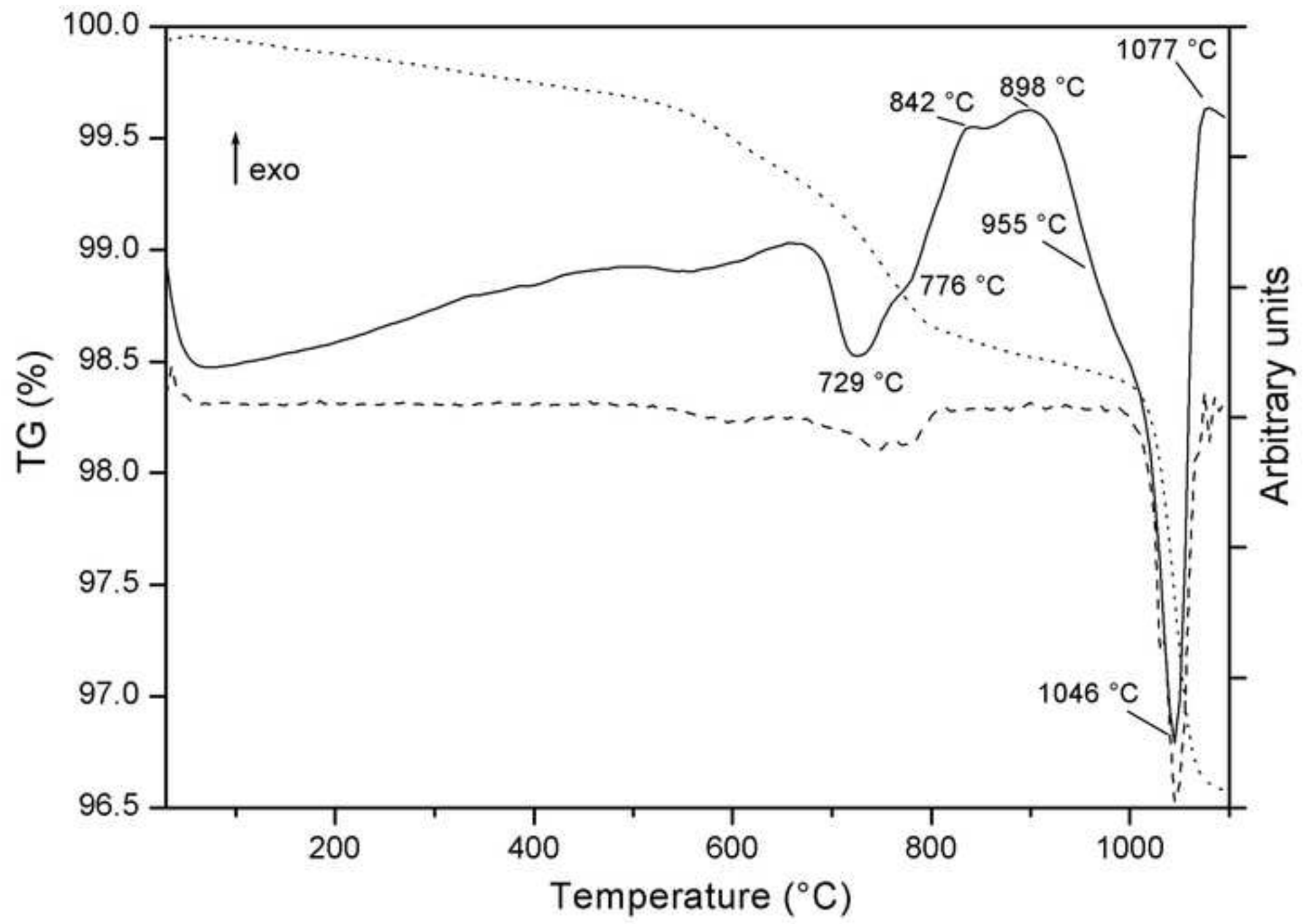


Fig.11

[Click here to download Figure: Fig. 11.tif](#)

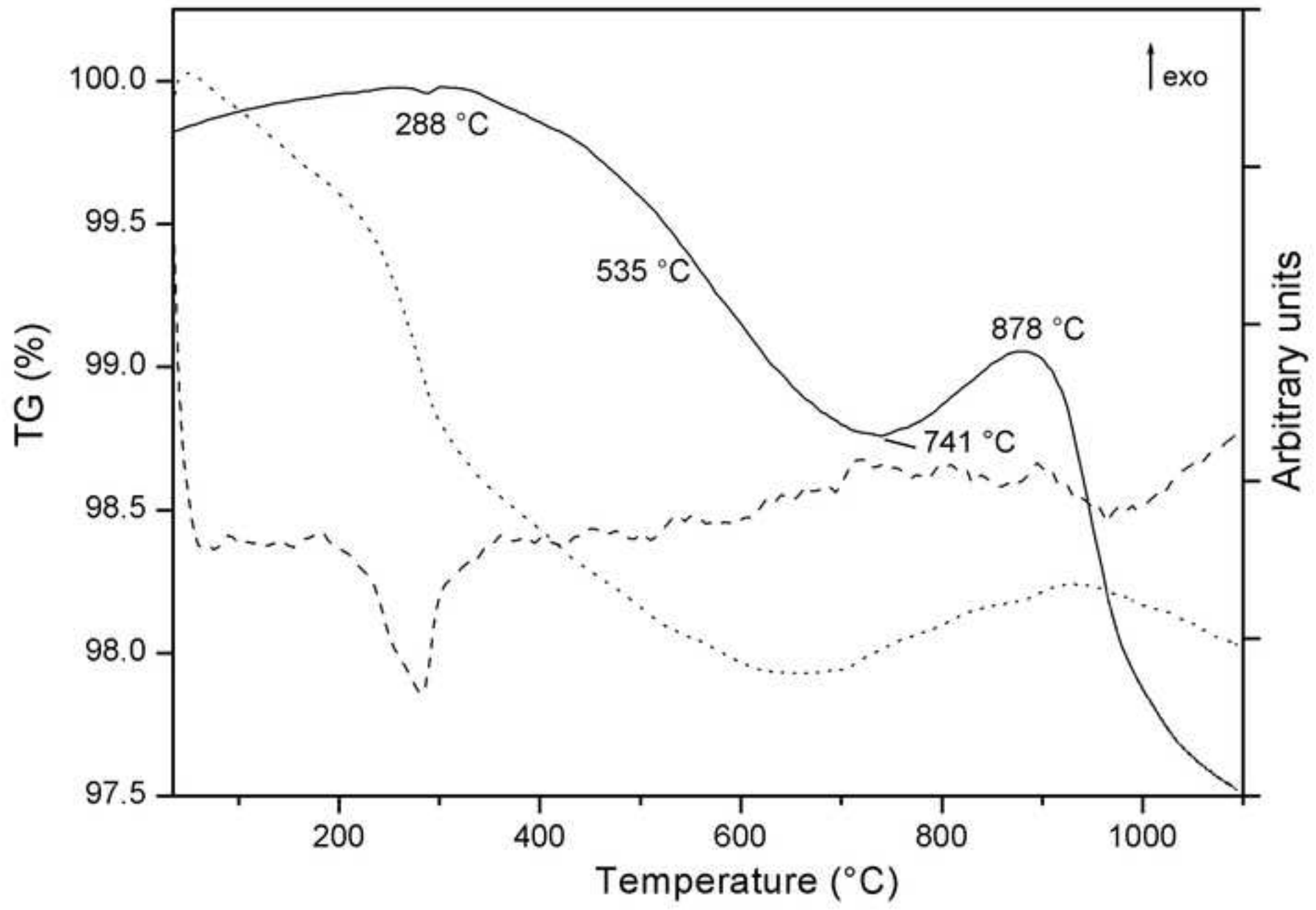


Fig.12

[Click here to download Figure: Fig. 12.tif](#)

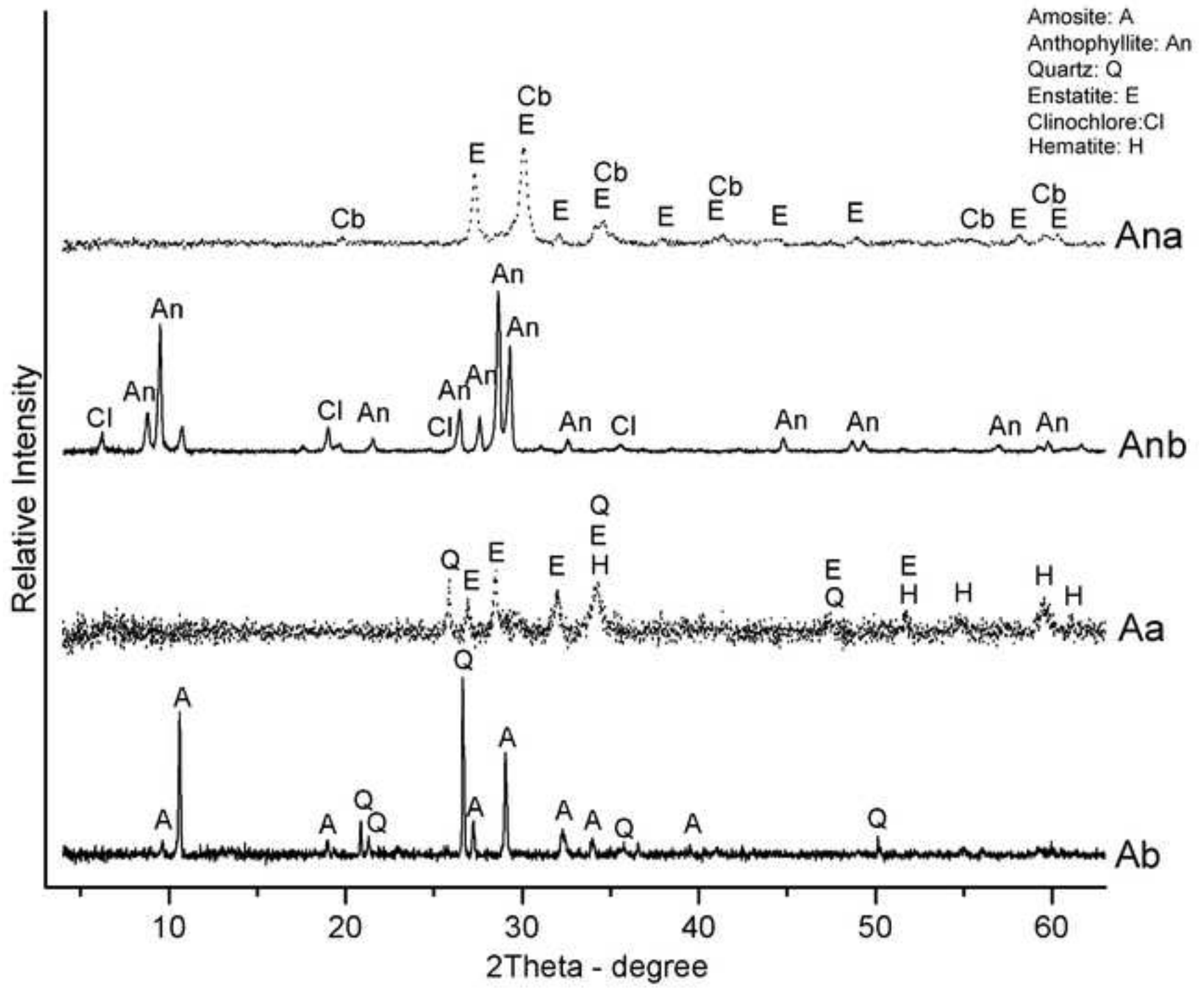


Fig.13

[Click here to download Figure: Fig. 13.tif](#)

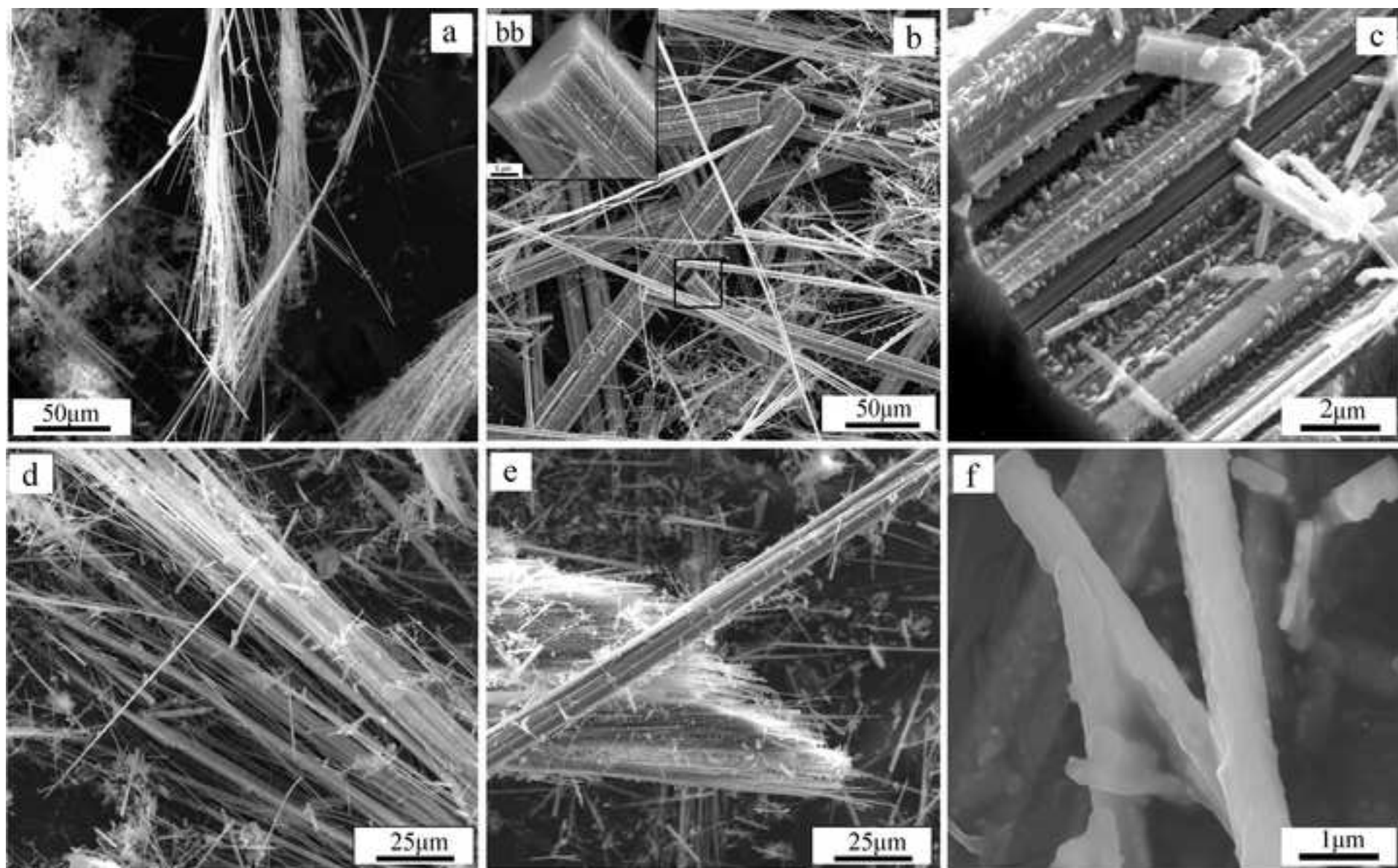


Fig.14

[Click here to download Figure: Fig. 14.tif](#)

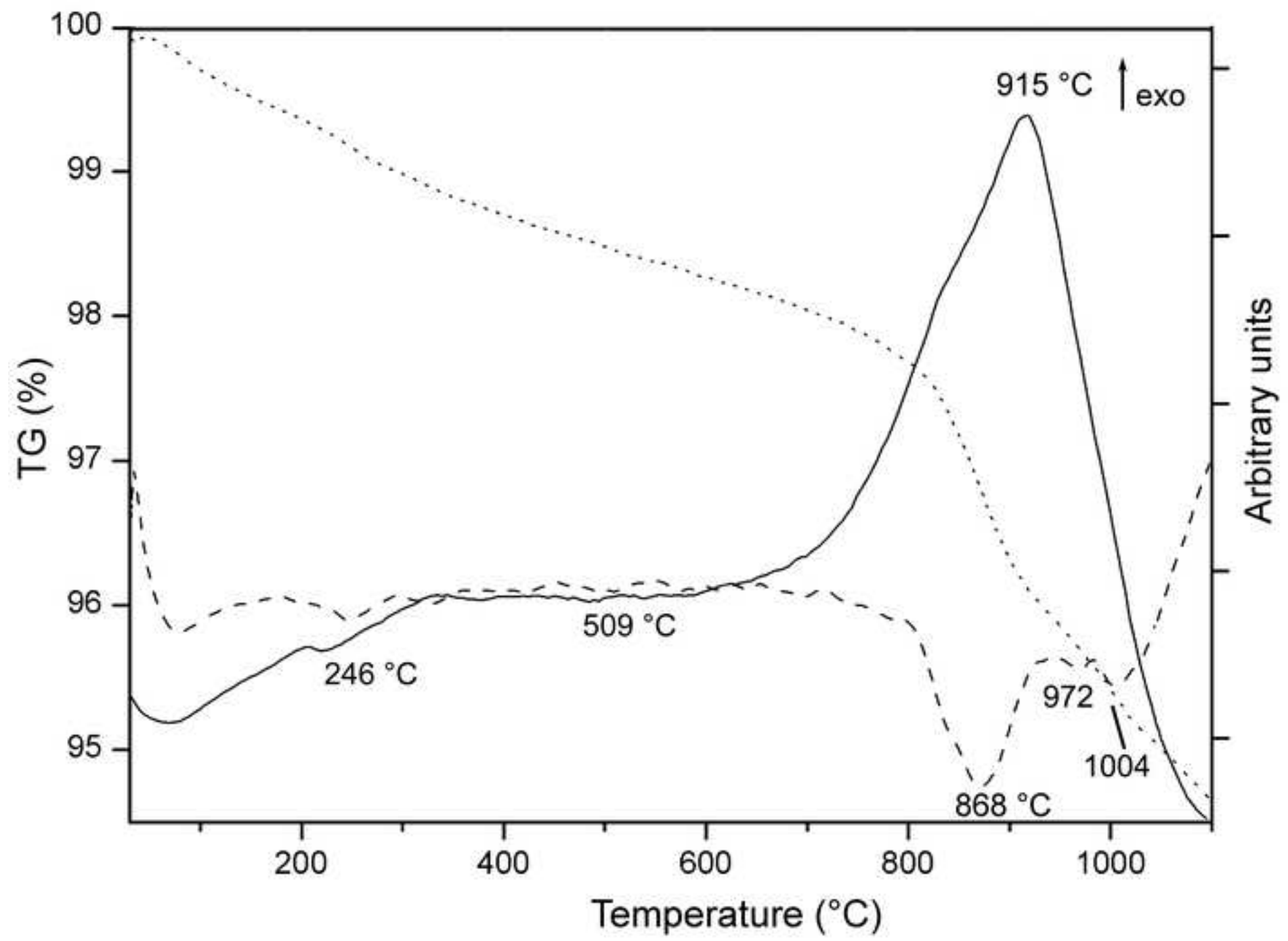


Fig.15

[Click here to download Figure: Fig. 15.tif](#)

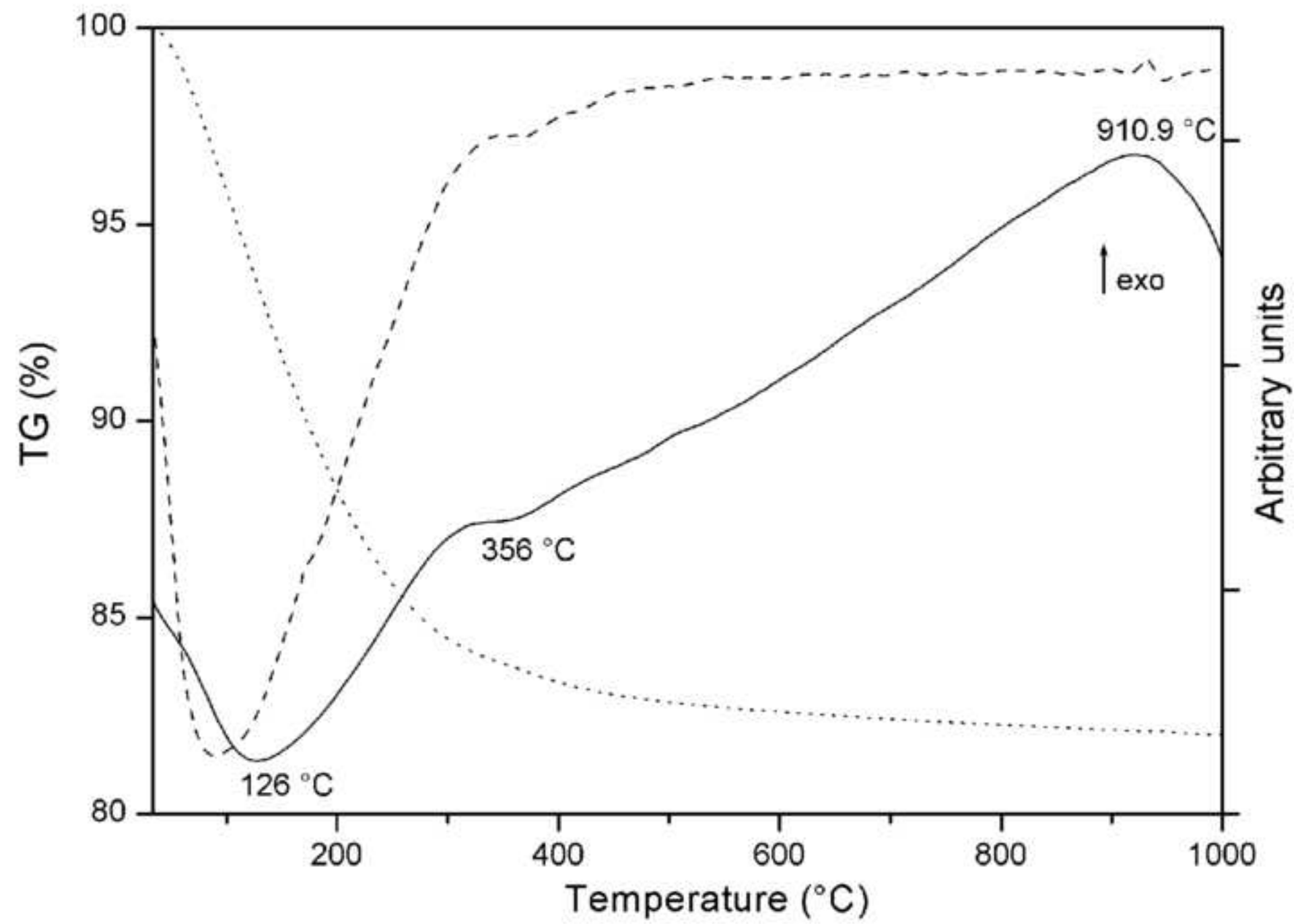


Fig.17

[Click here to download Figure: Fig. 17.tif](#)

